Journal of Materials Research and Technology 42 (2026) 9006–9021

Contents lists available at ScienceDirect

Journal of Materials Research and Technology

journal homepage: www.elsevier.com/locate/jmrt

Influence of build orientation and heat treatment on mechanical, tribological, and corrosion performance of LPBF Inconel 625

Danijela A. Skobir Balantič *, Črtomir Donik, Bojan Podgornik, Aleksandra Kocijan, Matjaž Godec

Institute of Metals and Technology, Lepi pot 11, 1000, Ljubljana, Slovenia

ARTICLE INFO

Keywords:
Inconel 625
Additive manufacturing
Build orientation
Strength
Impact toughness
Wear
Corrosion behaviour

ABSTRACT

This study examines the influence of build orientation and post-processing heat treatments on the microstructure and properties of laser powder bed fused (LPBF) Inconel 625 (IN625), with conventionally manufactured material used as a reference. The as-built alloy exhibits a highly anisotropic microstructure composed of elongated columnar grains, a fine cellular/dendritic substructure, and high dislocation density. Vertically built specimens show greater columnar continuity than horizontally built ones, resulting in pronounced mechanical anisotropy.

Stress-relief annealing at 870 °C reduces residual stresses through recovery, while preserving the solidification microstructure without recrystallisation. Solution annealing at 1050 °C promotes microstructural homogenization by dissolving segregation-related phases and partial recrystallisation. Recrystallisation is orientation-dependent and more extensive in horizontally built specimens, leading to lower dislocation density and a more equiaxed grain structure, while vertically built material retains elements of the columnar architecture.

These microstructural changes directly affect performance. Horizontally built specimens exhibit higher yield and tensile strengths, whereas vertically built specimens show superior ductility and impact toughness. Corrosion resistance improves progressively with heat-treatment temperature, with solution annealing achieving near-conventional performance due to enhanced chemical homogeneity. Although the as-built condition shows higher strength and hardness, it suffers from increased wear associated with brittle behaviour; heat treatments reduce wear anisotropy, with solution annealing providing the highest wear resistance.

LPBF IN625 responds non-uniformly to conventional heat treatments, and build orientation plays a critical role in controlling recrystallisation kinetics and property anisotropy, providing guidance for optimised post-processing strategies.

1. Introduction

Inconel 625 is one of the nickel-based superalloys, where the solid solution strengthening is reached by solving Nb and Mo atoms in a Ni–Cr matrix [1,2]. Due to its outstanding combination of high yield, tensile, and creep strengths, excellent high-temperature performance, weldability, and resistance to prolonged high-temperature corrosion in harsh environments, this material has gained a lot of attention in the aerospace, marine, chemical and nuclear industries [3]. It has been widely used for producing engine components, heat exchangers, and pressure valves [4–7]. The manufacturing of such components using a conventional manufacturing route, such as casting, forging or powder metallurgy is remarkably difficult, expensive and time-consuming due to the materials' properties characterised by high hardness, high-temperature strength and low thermal diffusivity [8–10].

Laser Powder Bed Fusion (LPBF) is a leading additive manufacturing (AM) technology that enables the fabrication of complex, high-performance metallic components, where the material can be deposited in a layer-by-layer manner to build the component [11,12]. In this process, a high-energy laser selectively melts regions of a powder bed according to a digital model, allowing for precise control over part geometry and microstructure [13,14].

The ability of nickel-based alloys for additive manufacturing is therefore of high potential and represents a significant step forward in producing near-net shape components with less material waste, time-efficient production and all that at lower costs [9,15,16]. However, during LPBF fabrication, Inconel 625 is exposed to repeated thermal cycling and steep, layer-by-layer thermal gradients. The orientation of a

* Corresponding author.
E-mail address: danijela.skobir@imt.si (D.A. Skobir Balantič).

https://doi.org/10.1016/j.jmrt.2026.05.163
Received 3 March 2026; Received in revised form 13 May 2026; Accepted 14 May 2026
Available online 15 May 2026

part during LPBF is another important aspect that dictates the direction of heat flow, the solidification front, and grain growth. These conditions promote the formation of complex microstructural features, including strong crystallographic texture and elongated epitaxial grains, which in turn introduce significant anisotropy [17]. LPBF IN625 also develops a fine cellular/dendritic substructure with Nb- and Mo- rich segregation at interdendritic regions and possible Laves phase formation.

The process parameters of LPBF critically influence microstructural features, including grain size, texture, and phase precipitation, which in turn govern key mechanical properties such as tensile strength, ductility, and anisotropy. Optimising these parameters is therefore essential to reduce defects, including porosity and cracks, control microstructural evolution, and enhance overall mechanical performance [18–20]. Consequently, numerous studies have investigated the effects of laser power, scanning speed, hatch spacing, and layer thickness on the microstructure and, subsequently, the material properties of LPBF-fabricated Inconel 625 components. Marchese et al. [21] examined how different parameter combinations influence densification and Brinell hardness while Yadroitsev et al. [22] focused primarily on the effects of varying hatching distances and scanning strategies on the density. They also reported that as-built IN625 specimens exhibit higher tensile strength but reduced ductility compared to the wrought IN625 alloy. In addition to process parameters, post-processing heat treatment is essential for achieving optimal mechanical performance in additively manufactured components [23,24]. Proper heat treatment reduces residual stresses, mitigates elemental segregation, and facilitates controlled grain growth and phase precipitation. Through these mechanisms, it enables the formation of tailored microstructures and mechanical properties suited to specific service conditions, thereby enhancing the material's overall reliability and functionality. For example, Li et al. [25] examined the microstructure, texture, grain morphology, and hardness of as-built and short-term heat-treated IN625 specimens. Brown et al. [26] investigated the tensile properties of stress-relieved IN625 specimens produced using different LPBF machines, demonstrating that variations in building strategies and associated thermal histories can lead to significant differences in tensile behaviour.

However, as recently highlighted by several authors [13,27,28], the mechanical behaviour of LPBF-fabricated IN625 components is strongly influenced by the interplay between build orientation, process parameters, and post-processing heat treatment. Because the build angle determines melt-pool boundary alignment, defect orientation, thermal gradient direction, and grain growth pathways, together, these factors govern the material's anisotropic properties, affecting mechanical, tribological, and corrosion performance. Several studies have specifically addressed the effect of build orientation on the mechanical behaviour of AM-fabricated IN625. For instance, Liu et al. [13] investigated the anisotropy of tensile properties at different test temperatures and build orientations, reporting the highest tensile strength at a 0° orientation, whereas specimens built at 90° exhibited the greatest elongation. Poulin et al. [28] examined fatigue crack propagation in LPBF IN625 as a function of build orientation and post-processing conditions. Yan et al. [27] presented the influence of build orientations on the surface properties and tribological performance. Since LPBF surface roughness is strongly linked to melt-pool geometry and scan path, orientation inherently alters asperity distribution, which affects friction and wear behaviour. Despite these efforts, investigations of orientation-dependent properties remain limited, and available data are often extrapolated from studies on other Inconel alloys, predominantly IN718 [29,30]. In particular, orientation-dependent tribological and corrosion behaviour of LPBF IN625 remains insufficiently studied, with only a few works addressing wear [31,32] and almost none examining corrosion [33] as a function of build orientation.

The present study addresses a gap in the literature by investigating the influence of build orientation and post heat-treatments on the tribological and corrosion behaviour, as well as the mechanical performance of the material, including impact toughness at room and elevated temperatures. To enable a comprehensive performance comparison, all analyses were also conducted on conventionally manufactured IN625 alloy.

2. Experimental

2.1. Material and processing

Commercially available gas-atomised powder with an average particle size of 45 ± 15 μm from EOS GmbH was used to manufacture the LPBF-manufactured IN625 blocks. LPBF process was performed on an industrial EOSINT M280 machine using commercial process parameters: fibre-laser power of 300 W, beam diameter of 0.11 mm, scan speed of 990 mm/s, distance between laser paths of 0.11 mm, and overlapping between laser paths of 0.08 mm. A meandering scanning strategy was employed, with the scanning direction rotated by 67° between successive layers. This rotation helps minimise microstructural anisotropy and promotes a more uniform thermal distribution across the build parts. The blocks of dimensions of 12 mm × 12 mm × 65 mm were built in two build orientations: horizontal/parallel (X) and vertical/perpendicular (Z) orientations (Fig. 1a). For comparative analysis, IN625 specimens fabricated via conventional casting and forging methods were also included in the study. The chemical compositions of the as-built additive-manufactured (AM) and conventionally produced (CM) specimens are presented in Table 1.

Investigations of the AM material were conducted in the as-built condition and after two distinct heat treatments. The first heat treatment, stress-relief (SR) annealing at 870 °C for 1 h, was performed to reduce residual stresses induced during the additive manufacturing process. The second heat treatment, solution annealing (ST) at 1050 °C for 1 h, was carried out to homogenise the microstructure and dissolve precipitates. The heat treatment of the reference CM IN625 specimens consisted only of solution annealing at 1050 °C for 1 h, which is considered the initial state of this material. After the heat treatment, all specimens were water-quenched to prevent microstructural changes during cooling. Table 2 summarises all specimens included in this investigation, along with their processing conditions and build orientation. For further experimental analyses, various specimen types were prepared from printed blocks to meet the requirements of the individual test procedures.

2.2. Microstructural characterisation

Microstructural characterisation of all specimens was performed on cross-sectioned specimens using an optical microscope (OM) and scanning electron microscopy (SEM). Specimens were prepared according to standard metallographic procedures (embedding in a conductive Bakelite resin, grinding, and polishing) and etched with a reagent consisting of 30 mL lactic acid, 20 mL hydrochloric acid (HCl), and 10 mL nitric acid (HNO_3) to reveal the microstructure, especially melt pools. Specimens for the in-plane views were etched using a combined procedure of classical chemical and ion etching to enhance microstructural contrast. Ion etching was performed using a PECS system (Gatan) at an ion beam current of 400 mA and an accelerating voltage of 10 keV for 10 min. Specimens prepared for EBSD were initially polished with diamond suspensions to 1 μm, and subsequently OPS (40 nm SiO_2 oxide) polished for 30 min. Optical microscopy was performed using a ZEISS Axio Imager Z2m – Metallographic Optical Microscope. SEM analysis was carried out on a ZEISS CrossBeam 550 FIB SEM with an EDAX Hikari Super EBSD camera, using APEX software and EBSD post-processing using OIM 9.1. SEM/EBSD was performed using 15 kV accelerating voltage, 2.0-5.0 nA probe current for SE imaging and 10 nA probe current on 70°-tilted specimens for EBSD. The quantitative EBSD analysis was performed on three fields of view, each 400 μm × 400 μm. The fracture surfaces resulting from Charpy impact toughness tests were also

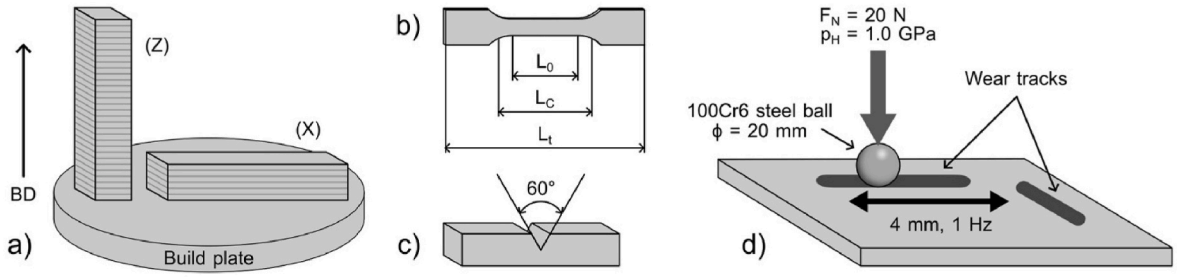

Fig. 1. (a) Build orientations of LPBF specimens; the geometry of (b) tensile specimens, (c) Charpy V-notched specimens and (d) configuration of the tribological test set-up.

Table 1
Chemical compositions of the investigated IN625 specimens (in wt.%).

	C	Si	Mn	S	Cr	Mo	Nb	Fe	Ti	P	Ni
AM IN625	0.010	0.35	0.037	0.004	20.5	8.8	3.8	0.78	0.36	<0.01	Bal.
CM IN625	0.009	0.34	0.047	0.002	21.2	8.1	3.2	5.0	0.13	<0.01	Bal.

Table 2
Specimen labels with described processing conditions, and build orientation.

Specimen Label	Specimen condition	Build orientation
CM	Conv. manufactured + solution annealed at 1050 °C/1h	
AM-AB-H	Additive manufactured (AM) as-built	horizontal (X)
AM-AB-V	Additive manufactured (AM) as-built	vertical (Z)
AM-SR-H	AM as-built + stress-relief (SR) annealed at 870 °C/1h	horizontal (X)
AM-SR-V	AM as-built + stress-relief (SR) annealed at 870 °C/1h	vertical (Z)
AM-ST-H	AM as-built + solution annealed (ST) at 1050 °C/1h	horizontal (X)
AM-ST-V	AM as-built + solution annealed (ST) at 1050 °C/1h	vertical (Z)

analysed using SEM.

Electron Channelling Contrast Imaging (ECCI) was used to characterise dislocation structures, sub-grain features, and precipitate distributions in bulk specimens. This technique was chosen for its ability to provide high-resolution microstructural information over large areas with minimal sample preparation, offering advantages compared with conventional electron backscatter diffraction (EBSD). ECCI observations were performed using a scanning electron microscope equipped with an electron backscatter diffraction detector, operated at an accelerating voltage of 15 kV and a probe current of 2 nA.

2.3. Mechanical and tribological performance

Flat tensile specimens (Fig. 1b) were machined according to DIN50125:2022 (Type E) [34] and tested according to EN ISO 6892-1:2019 [35] for uniaxial tensile testing, ensuring appropriate geometry and surface finish for accurate determination of mechanical properties. Tensile tests at room temperature were carried out to determine the yield strength (YS), ultimate tensile strength (UTS) and elongation (EL). The experiments were performed on a ±250 kN dynamic testing machine (INSTRON 8802, Zwick/Roell Retro Line).

Standard Charpy V-notch (CVN) specimens (Fig. 1c) were fabricated and tested in accordance with ISO 148-1:2016 [36] to evaluate the impact toughness of the investigated material. For horizontally built specimens, the V-notch was oriented parallel to the building direction, whereas in vertically built specimens, all sides of the square cross-section were equivalent. The tests were conducted at room temperature and at elevated temperatures of 650 °C, 750 °C, and 850 °C using a Charpy impact testing machine equipped with a 300 J pendulum. The elevated temperatures selected for impact testing correspond to typical service temperature ranges of IN625 in aerospace and energy applications. Tensile and wear tests were conducted at room temperature to isolate the influence of build orientation and heat treatment from thermally activated deformation mechanisms and oxidation-assisted wear effects.

Hardness measurements were performed on cross-sections of horizontally and vertically built blocks using an Innovates Falcon 800G2A03 Vickers hardness tester under a 10 kg load (HV10) to assess surface hardness.

Wear and corrosion specimens were prepared from the cross-sections as well, with dimensions of 12 mm × 12 mm × 5 mm. Dry-sliding wear tests were conducted to evaluate wear resistance and the coefficient of friction as a function of heat treatment and build orientation. The experiments were performed in reciprocating sliding mode (a = 4 mm, f = 1 Hz) using a ball-on-flat configuration (Fig. 1d). To minimise the influence of surface roughness, all specimens were mirror-polished to an average surface roughness Ra of 0.05 μm. Prior to testing, specimens were ultrasonically cleaned in ethanol and air-dried. For wear testing, a 20 mm diameter 100Cr6 hardened bearing steel ball (58 HRC) was employed as the oscillating counter-body. Tests were carried out under the following conditions: room temperature, 50% relative humidity, average sliding speed of 0.01 m/s, normal load of 20 N (corresponding to a nominal contact pressure of 1.0 GPa), and a total sliding distance of 5 m. Sliding tests on all AM specimens (horizontally and vertically built ones) were performed parallel and perpendicular to the layer's orientation. During testing, the coefficient of friction was continuously recorded as a function of sliding distance, and the average steady-state value determined. Wear tracks and volumes were quantified using an Alicona InfiniteFocus G4 high-resolution 3D confocal focus variation microscope.

In all mechanical and tribological performance, at least three replicate tests were carried out to ensure statistical reliability of the results.

2.4. Electrochemical performance

Potentiodynamic polarisation curves were measured in a 3.5% NaCl solution at room temperature using a BioLogic® SP-300 potentiostat/galvanostat/FRA controlled by EC-Lab® V11.27 software. A conventional three-electrode electrochemical cell was employed, with the test specimen as the working electrode, a saturated calomel electrode (−SCE, 0.242 V vs. SHE) as the reference electrode, and a platinum mesh as the counter electrode. Prior to measurements, the specimens were

stabilised at the open-circuit potential for 1 h. The scan rate was 1 mV/s. All experiments were performed in triplicate to ensure statistical reliability.

3. Results and discussion

3.1. Microstructure

Optical microscopy (OM) images of the conventionally produced material, as well as the horizontally and vertically built LPBF specimens in their as-built and heat-treated conditions, are shown in Fig. 2. The conventionally produced material, solution-annealed at 1050 °C (Fig. 2a), exhibits a fully recrystallised γ (FCC) matrix with large equiaxed austenitic grains. In contrast, the as-built LPBF IN625 (Fig. 2b) reveals a highly heterogeneous microstructure, characterised by overlapping melt pools with well-defined boundaries and columnar grains aligned along the build direction. These columnar grains, formed by rapid cooling and directional solidification inherent to the LPBF process, consist of fine cellular or dendritic substructures, consistent with previous reports [4,25,37]. After stress-relief annealing at 870 °C (Fig. 2c), no visible changes in the microstructure are observed. The melt pool morphology and dendritic substructure remain intact, indicating that this heat treatment does not eliminate solidification-related features. The microstructure remains primarily governed by the LPBF process's thermal history. Solution annealing at 1050 °C (Fig. 2d) leads to pronounced microstructural changes. At this temperature, recrystallisation and grain growth remove the melt-pool boundaries and dissolve the dendritic substructure, resulting in a more homogeneous microstructure that closely resembles that of conventionally processed material. Similar microstructural features are observed for the vertically built specimens in both the as-built and heat-treated states (Fig. 2b1, 2c1, and 2d1). In terms of build orientation, no major differences in microstructure are detected between horizontal and vertical build orientations, except for the melt pool width. In horizontally built specimens, the melt pool width is approximately 130 μm, while in vertically built ones, it reaches about 140 μm and appears more elongated. Due to overlapping melt pools, however, these measurements are only approximate.

The in-plane (top-view) image of the as-built microstructure clearly reveals the printing pattern, with individual laser scan tracks and the applied rotation angle distinctly visible (Fig. 3a). This scanning strategy is directly reflected in the resulting microstructure, where grains exhibit a pronounced preferential alignment along the laser paths (Fig. 3b). The higher-magnification image (Fig. 3c) shows a substructure composed of both columnar dendrites and equiaxed grains.

Fig. 4 presents representative SEM micrographs of LPBF-fabricated IN625 specimens under all investigated conditions and build orientations. In the as-built state, specimens from both orientations (Fig. 4a and b) exhibit the characteristic melt pool morphology with overlapping scan tracks, reflecting the layer-by-layer thermal cycling inherent to the LPBF process. Melt pool boundaries are clearly visible in both orientations, appearing as arc-shaped regions in horizontally built specimens and as stacked, elongated pools in vertically built ones. The melt pool geometry in vertically fabricated specimens is notably more elongated along the build direction, indicating a strong directional heat flow during solidification.

Micrographs of higher magnification (Fig. 4a1 and 4b1) reveal that the microstructure is dominated by a fine cellular and columnar/dendritic solidification substructure, with cell sizes ranging from the submicron scale to approximately 1 μm. This morphology is characteristic of rapidly solidified Ni-based superalloys produced via LPBF and results from the combination of high cooling rates and steep thermal gradients during processing. Microsegregation is expected to result in local enrichment of Nb and Mo, which may promote the formation of Laves phase along cell boundaries, as reported for LPBF IN625 [38]. However, the presence of the Laves phase in the present study is inferred based on typical solidification behaviour and cannot be directly confirmed at the current magnification.

A pronounced anisotropy and crystallographic texture associated with build orientation are clearly evident. In horizontally built specimens, the cellular structure appears more equiaxed, whereas in vertically built specimens, cells and columnar features are preferentially aligned along the build direction. This reflects epitaxial grain growth across successive layers and the dominant heat extraction along the build axis. Such orientation-dependent microstructural characteristics are well documented and are known to contribute significantly to the anisotropic mechanical behaviour of LPBF-processed IN625. Following stress-relief heat treatment at 870 °C for 1 h, the overall melt-pool architecture and cellular solidification substructure are largely preserved in both build orientations, as shown in Fig. 4c and d. No evidence of recrystallisation is observed; the microstructure retains its columnar morphology and melt pool pattern, although with slightly reduced subgrain contrast, consistent with recovery rather than recrystallisation. This suggests that the applied temperature and duration are insufficient to trigger substantial recrystallisation or notable grain boundary migration.

At higher magnification (Fig. 4c1 and 4d1), several notable changes become apparent. The cellular boundaries are less sharply defined compared to the as-built condition, indicating partial homogenization of elemental segregation. Additionally, fine plate-like or needle-like precipitates are observed, primarily along former interdendritic or intercellular regions. Based on their morphology, location along interdendritic regions, and the applied heat-treatment temperature range, they are tentatively attributed to the formation of the δ phase (Ni_3Nb), rather than to retained or newly formed Laves phase [39,40].

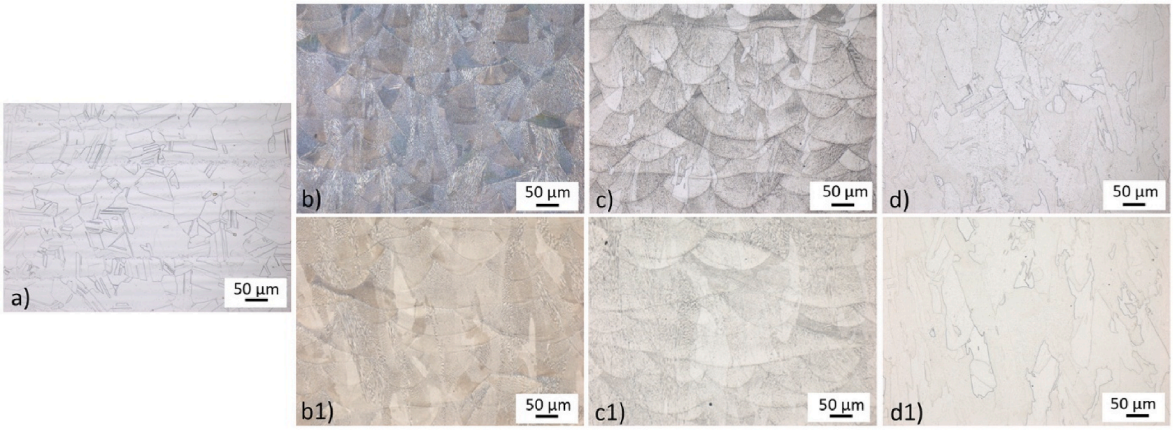

Fig. 2. OM images of IN625 specimens: (a) CM, (b) AM-AB-H, (c) AM-SR-H, (d) AM-ST-H, (b1) AM-AB-V, (c1) AM-SR-V, and (d1) AM-ST-V.

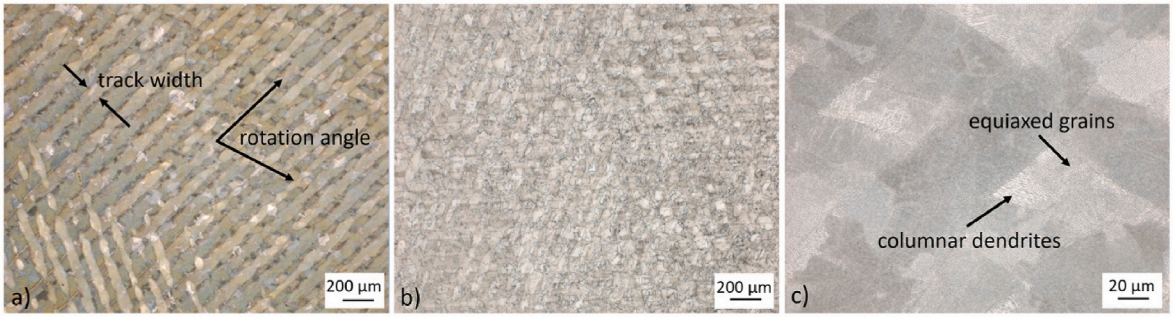

Fig. 3. OM images (in-plane) of as-built IN625: (a) classical etched, (b) classical + ion etched, (c) higher magnification image.

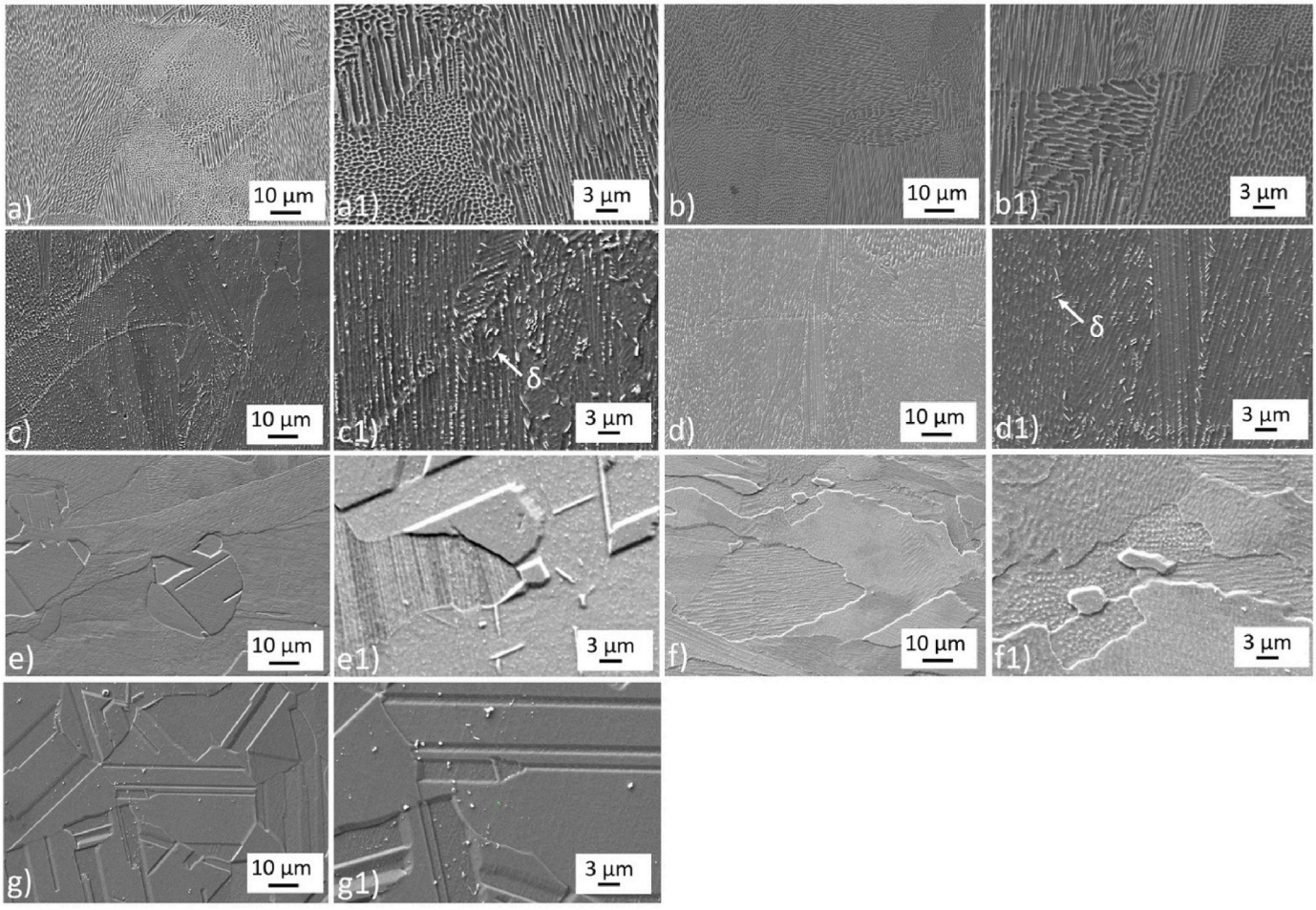

Fig. 4. SEM micrographs of IN625 specimens: (a) AM-AB-H, (b) AM-AB-V, (c) AM-SR-H, (d) AM-SR-V, (e) AM-ST-H, (f) AM-ST-V, (g) CM. Images (a1), (b1), (c1), (d1), (f1) and (g1) correspond to higher-magnification images of the same specimens, respectively.

Although Nb-rich Laves phase typically forms during solidification in the as-built condition, it becomes thermodynamically unstable at temperatures approaching 870 °C and is expected to partially dissolve during stress-relief annealing. The subsequent redistribution of Nb promotes δ-phase precipitation within the temperature range of approximately 650–900 °C [41,42].

The vertically built, stress-relieved specimen exhibits slightly higher density and greater continuity of δ-phase precipitates than its horizontally built counterpart. This is likely due to enhanced Nb segregation associated with columnar grain growth along the build direction, which locally increases the driving force for δ-phase formation. Importantly, the persistence of the cellular framework confirms that stress relief is primarily focused toward reduced residual stresses and alters the distribution of secondary phases without fundamentally changing the solidification microstructure established during LPBF processing.

The solution-annealed specimens, treated at 1050 °C for 1 h, exhibit a markedly different microstructure. At low magnification (Fig. 4e and f), the melt pool boundaries and solidification-related features visible in the as-built and stress-relieved conditions are no longer discernible. Instead, the microstructure is dominated by large, equiaxed grains, closely resembling those found in conventionally wrought material, indicative of extensive recrystallisation and grain growth. High-magnification images (Fig. 4e1 and 4f1) reveal relatively homogeneous grain structures, confirming the effective dissolution of the

cellular substructure and elemental segregation. The fine precipitates observed after stress-relief treatment are absent, consistent with the expected dissolution of segregation-induced phases such as Laves and δ phases at elevated temperatures [43]. Occasional grain-boundary features remain and are likely attributable to stable carbides that persist in IN625 even after solution annealing.

Following solution annealing, the differences between the horizontal and vertical build orientations are significantly diminished. Both grain morphology and size distribution appear comparable, demonstrating that high-temperature treatment effectively eliminates the microstructural anisotropy introduced during LPBF processing. The microstructure of conventionally produced IN625 (Fig. 4g and g1) exhibits typical wrought characteristics, including grain-boundary carbide precipitation within a γ-matrix, along with a limited number of intragranular carbide particles. Solution annealing at 1050 °C leads to the dissolution of chromium-rich $M_{23}C_6$ carbides, while Nb-rich carbides only partially dissolve and remain discontinuously distributed along grain boundaries. This reduction in carbide content contributes to a more homogeneous

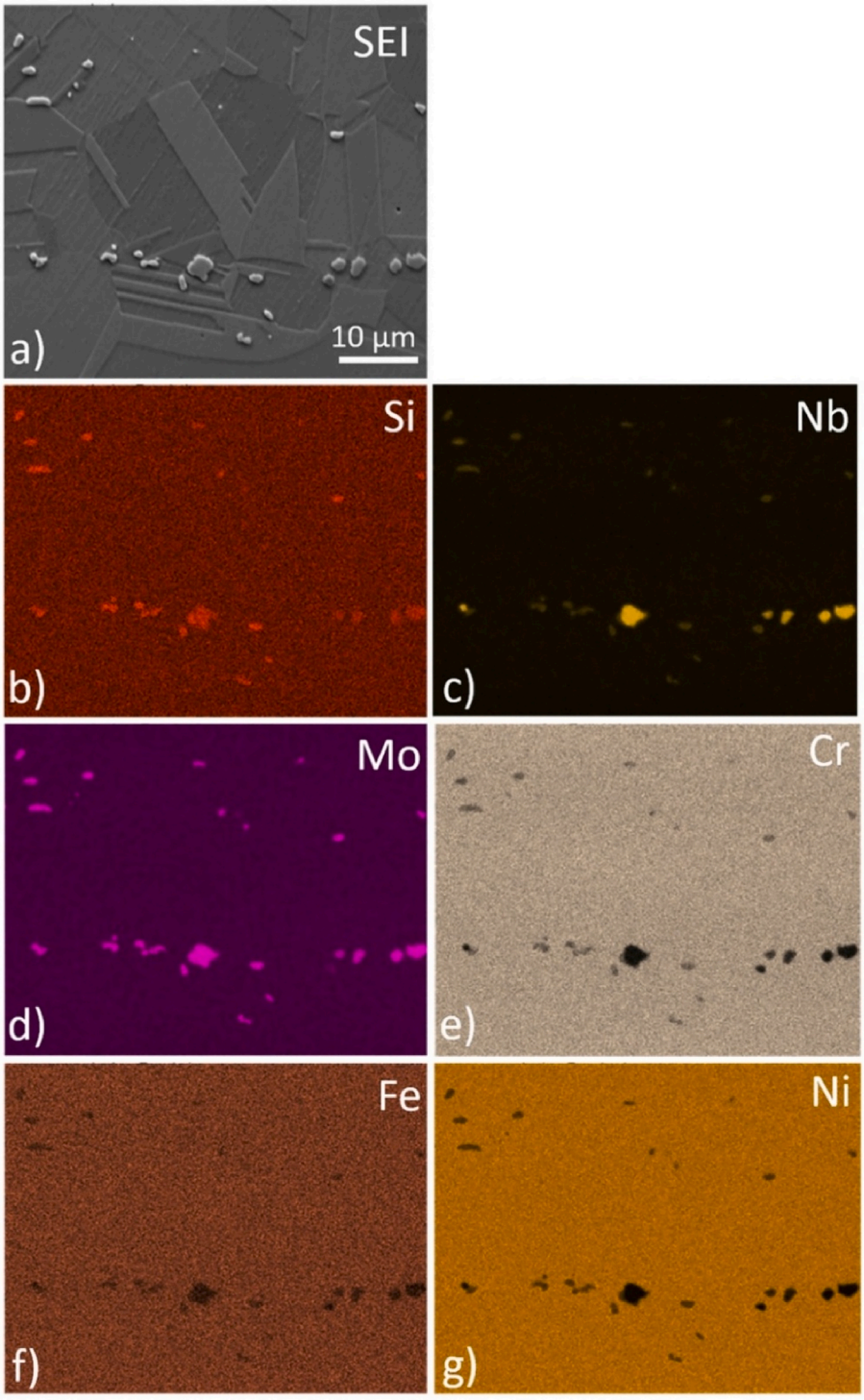

Fig. 5. (a) SE image of conventional IN625 with corresponding elemental EDS maps showing the distribution of key alloying elements: (b) Si, (c) Nb, (d) Mo, (e) Cr, (f) Fe and (g) Ni.

microstructure, which is beneficial for mechanical performance [44]. No δ or Laves phases are detected in conventional IN625 after solution annealing, indicating effective homogenization during high-temperature processing. Although not all carbides are clearly resolvable at this magnification, the uniform etched contrast and absence of interdendritic features confirm the presence of a homogenised, single-phase γ-matrix.

The microstructural evolution observed across the three conditions underscores the critical role of post-processing heat treatments in controlling phase stability and anisotropy in LPBF-fabricated IN625. In the as-built state, the material exhibits a highly anisotropic, segregation-rich cellular structure that is strongly influenced by build orientation. Stress-relief annealing at 870 °C preserves this architecture while promoting δ-phase precipitation along Nb-enriched cell boundaries, especially for vertical building direction, which can affect the material's mechanical behaviour. In contrast, solution annealing at 1050 °C leads to near-complete microstructural homogenization, including the dissolution of segregation-induced phases and the elimination of build-orientation-dependent features. These findings indicate that while stress-relief treatment effectively reduces residual stresses, it does not eliminate the solidification-induced anisotropy. Therefore, achieving isotropic microstructure requires high-temperature solution annealing. The results demonstrate that the interplay between LPBF-induced microsegregation, build orientation, and post-processing heat treatments governs phase evolution and anisotropy in IN625, with δ-phase precipitation contributing to microstructural stabilisation.

Fig. 5 presents a secondary electron (SE) micrograph and the corresponding EDS elemental maps of conventionally processed Inconel 625 after solution annealing at 1050 °C for 1 h. The SE image reveals a fully recrystallised microstructure consisting of equiaxed γ grains and a population of bright, angular particles distributed along former grain boundaries and within grain interiors. These particles exhibit strong compositional contrast relative to the matrix. The EDS elemental maps indicate pronounced enrichment of Nb and Mo at the locations of the bright particles, suggesting the presence of Nb- and Mo-rich secondary phases, most likely carbides commonly reported in wrought IN625 [45]. In contrast, the Ni, Cr and Fe maps show a largely homogeneous distribution throughout the matrix, consistent with a γ-Ni solid solution. The Si map likewise exhibits a predominantly uniform background, indicating that silicon is mainly dissolved in the matrix, although minor

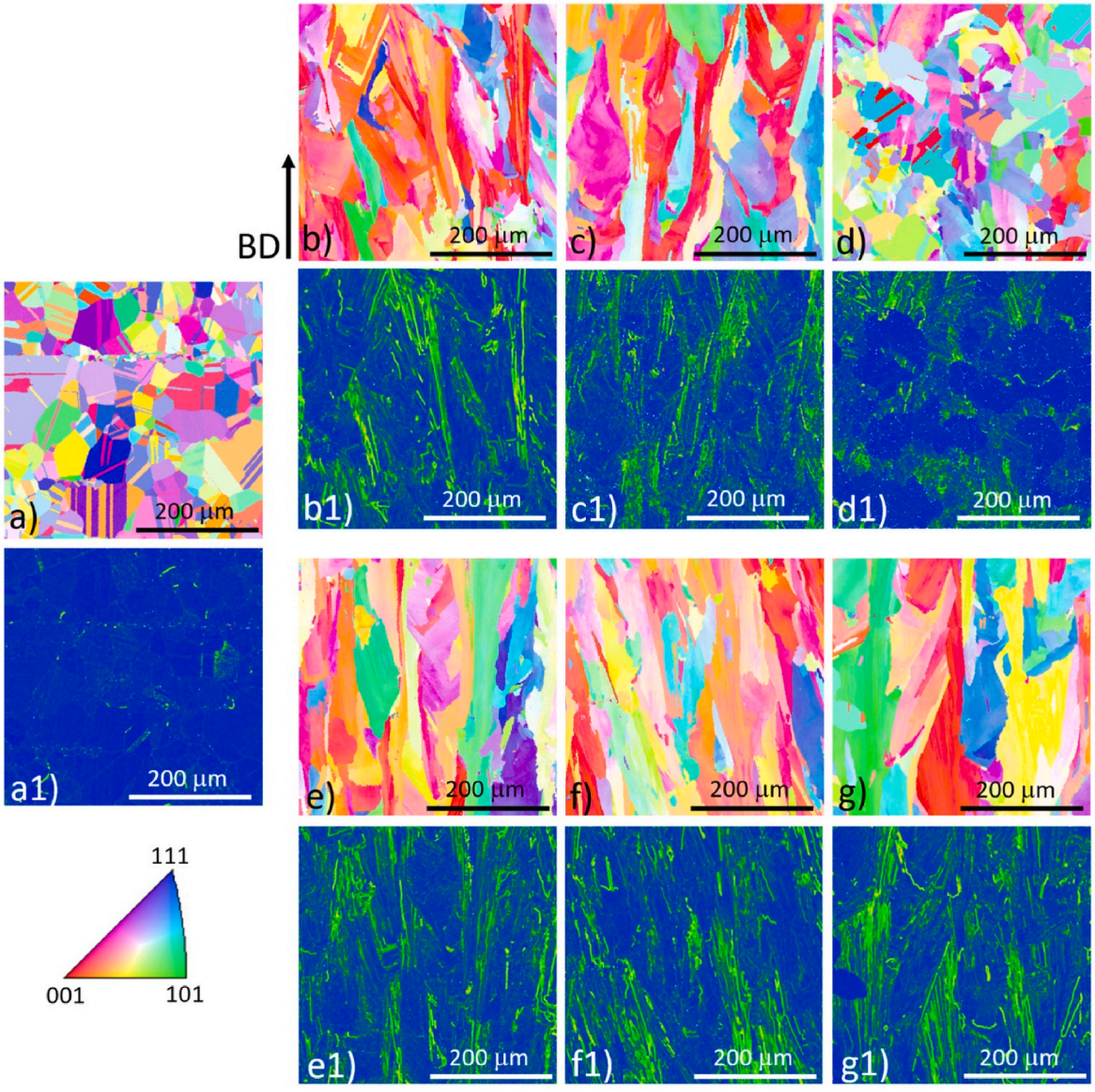

Fig. 6. EBSD IPF maps in the Z direction of IN625 specimens: (a) CM, (b) AM-AB-H, (c) AM-SR-H, (d) AM-ST-H, (e) AM-AB-V, (f) AM-SR-V, and (g) AM-ST-V. Fig. (a1), (b1), (c1), (d1), (e1), (f1), (g1) present the corresponding KAM maps, respectively.

localised enrichment at some precipitate sites cannot be excluded. The EDS results confirm a microstructural state typical of solution-annealed IN625, characterised by a predominantly single-phase γ matrix with a limited fraction of Nb- and Mo-rich precipitates. This elemental partitioning is consistent with the thermodynamic equilibrium expected under the applied heat-treatment conditions.

However, a direct comparison between additively manufactured (AM) and conventionally manufactured (CM) IN625 should be interpreted with caution, as the chemical compositions are not strictly identical, particularly with respect to Fe content (0.78 wt% in the AM material compared to 5.0 wt% in the CM material). Although Fe is not a primary strengthening element in IN625 and does not destabilise the γ matrix, it can significantly influence phase stability and microstructural evolution [46]. Increased Fe content has been reported to enhance Nb and Mo segregation during solidification and to promote δ-phase precipitation during subsequent heat treatment, while also affecting the relative stability of Laves phases and carbide formation [47,48]. Although both materials fall within the nominal compositional range of IN625, such differences may still influence phase stability, precipitation behaviour, and, consequently, mechanical, tribological, and corrosion performance. Therefore, part of the observed differences between AM and CM specimens may arise not only from processing route and resulting microstructure, but also from compositional variations, particularly Fe-induced changes in solidification and precipitation behaviour.

Fig. 6 shows EBSD and corresponding KAM maps revealing differences in grain morphology, misorientation, and texture evolution between horizontally and vertically built LPBF IN625 specimens under various heat treatments, while Table 3 summarises the associated quantitative EBSD metrics, including grain size, grain boundary character distribution (LAGB/HAGB), recrystallised fraction, texture index, and average KAM values.

Fig. 6a presents the reference microstructure of conventionally processed IN625 after solution annealing at 1050 °C for 1 h. The EBSD orientation map reveals a fully recrystallised, equiaxed grain structure with weak crystallographic texture, while the corresponding KAM map shows uniformly low local misorientation values, indicating a very low dislocation density and near-complete relaxation of internal stresses. This condition represents an equilibrium microstructural state that is readily achieved in conventionally processed material under standard solution annealing conditions [49].

The LPBF-fabricated specimens exhibit a pronounced dependence of microstructural evolution on build orientation. In the as-built condition (Fig. 6b and e), both horizontally and vertically built specimens are characterised by elongated columnar grains aligned with the build direction and a strong crystallographic texture. However, the vertically built specimens display longer and more continuous columnar grains (Fig. 6e), whereas the horizontally built specimens show a more segmented columnar structure (Fig. 6b) due to frequent interruption of grain growth across layers. This difference is directly reflected in the KAM maps (Fig. 6b1 and 6e1), where vertically built specimens exhibit more continuous bands of high local misorientation, indicating a higher effective density of geometrically necessary dislocations and stronger residual stress accumulation.

Following stress relief annealing at 870 °C for 1 h (Fig. 6c and f), no significant changes in grain morphology are observed for either build orientation, confirming that this treatment primarily promotes recovery rather than recrystallisation. Nevertheless, a clear orientation-dependent response is evident in the KAM maps. Horizontally built specimens show a more pronounced reduction and fragmentation of high-KAM regions (Fig. 6c1), suggesting more effective dislocation rearrangement and stress relaxation. Vertically built specimens retain extended regions of elevated misorientation, indicating that recovery is less effective when the cellular substructure and columnar grains are aligned parallel to the build direction (Fig. 6f1).

Solution annealing at 1050 °C for 1 h induces partial recrystallisation in both LPBF configurations (Fig. 6d and g); however, the extent of recrystallisation is strongly orientation-dependent. Horizontally built specimens exhibit a higher fraction of equiaxed grains and a more substantial breakdown of the original columnar morphology. Correspondingly, their KAM maps (Fig. 6d1) show largely reduced misorientation with only localised residual high-KAM regions. Vertically built specimens retain pronounced elongated grains and continuous bands of elevated KAM even after solution annealing (Fig. 6g1). These features indicate persistent subgrain structures and localised dislocation accumulation, demonstrating that recrystallisation remains incomplete.

The quantitative EBSD analysis, summarised in Table 3, reveals a pronounced orientation-dependent recrystallisation behaviour after solution annealing. In horizontally built specimens (AM-ST-H), a high recrystallised fraction of approximately 90% (GAM 0–0.5°) is achieved, accompanied by a significant reduction in KAM values (2nd neighbour) and a decrease in texture intensity. This indicates an almost complete and spatially homogeneous recrystallisation, consistent with the change from the initial columnar grain structure to equiaxed grains observed in the EBSD maps (Fig. 6d). In contrast, vertically built specimens (AM-ST-V) exhibit a comparable average recrystallised fraction (~86%); however, the EBSD and corresponding KAM maps (Fig. 6g, g1) reveal a markedly heterogeneous microstructural state. Specifically, regions of fully recrystallised, low-KAM grains coexist with elongated bands of elevated local misorientation, indicating the persistence of deformation substructures and incomplete recrystallisation. This heterogeneity is not fully captured by the averaged EBSD metrics alone but becomes evident through spatially resolved analysis. The observed difference between build orientations can be attributed to the distinct grain morphologies and defect structures inherent to the LPBF process. Horizontally built specimens, characterised by a more fragmented columnar structure, provide a higher density of effective nucleation sites for recrystallisation, promoting a more uniform transformation. Conversely, the vertically built material retains long, continuous columnar grains aligned with the build direction, which limit nucleation, enhance Zener pinning, and reduce grain-boundary mobility [50,51]. As a result, recrystallisation proceeds locally rather than uniformly, leading to the coexistence of recrystallised and partially recovered.

These results demonstrate that LPBF IN625 does not respond uniformly to conventional heat-treatment protocols, and that build orientation plays a decisive role in controlling recrystallisation kinetics, dislocation annihilation, and residual-stress relaxation. Horizontally built specimens approach a more homogenised and recrystallised microstructure after solution annealing, whereas vertically built specimens retain a higher degree of inherited LPBF microstructural features, even under identical thermal conditions.

While EBSD and KAM maps (Fig. 6) provide insight into grain

Table 3
EBSD-derived microstructural parameters of the investigated specimens.

Specimen	KAM average	HAGB/LAGB	Recrystallised fraction (GAM) (%) 0-0.5°/0.5-2°/ > 2°	Texture index	Average grain size (μm^2)
CM	0.06 ± 0.01	35.29	100 ± 0/0/0	4.9 ± 0.9	420 ± 12
AM-AB-H	0.58 ± 0.03	2.50	65 ± 13/34 ± 13/0	8.0 ± 1.2	156 ± 18
AM-SR-H	0.54 ± 0.02	3.70	87 ± 14/12 ± 14/0	7.5 ± 1.1	156 ± 13
AM-ST-H	0.41 ± 0.03	3.93	90 ± 6/10 ± 6/0	4.5 ± 0.5	183 ± 7
AM-AB-V	0.52 ± 0.10	2.75	81 ± 17/19 ± 16/0	8.5 ± 0.9	134 ± 8
AM-SR-V	0.53 ± 0.03	2.72	81 ± 11/18 ± 11/0	8.4 ± 0.8	132 ± 9
AM-ST-V	0.46 ± 0.04	3.15	86 ± 3/14 ± 3/0	8.5 ± 1.5	165 ± 16

morphology, texture evolution, and local misorientation, ECCI analysis (Fig. 7) offers complementary information on the dislocation substructure and lattice strain distribution at a finer scale. The conventionally processed IN625 (CM) exhibits uniformly low ECCI contrast within equiaxed grains (Fig. 7a), consistent with the low KAM values observed in Fig. 6a1 and indicative of a nearly dislocation-free, fully recrystallised microstructure. The as-built LPBF specimens show pronounced, heterogeneous ECCI contrast (Fig. 7b and b1), reflecting a high density of stored dislocations and strong local lattice distortions consistent with the columnar grain morphology and orientation-dependent strain accumulation observed in the KAM maps (Fig. 6b1 and 6e1). Horizontally built specimens exhibit a more irregular contrast pattern, whereas vertically built specimens retain elongated columnar grains aligned with the build direction and a deformation-dominated substructure, consistent with the characteristic ⟨001⟩ texture of LPBF IN625 [13,52].

After stress-relief annealing at 870 °C, the ECCI contrast remains qualitatively similar to the as-built condition for both build orientations (Fig. 7c and c1), corroborating the EBSD/KAM results that indicate recovery-dominated behaviour without significant recrystallisation. A slight increase in nanoscale precipitate size is observed, mainly along dislocation cell walls, with features consistent with Cr-rich carbides and limited δ-phase formation (Fig. 7c and c1) [39,53,54]. Clear microstructural changes are only observed after solution annealing at 1050 °C. Horizontally built specimens exhibit extended regions of reduced ECCI contrast (Fig. 7d), consistent with a substantial reduction in dislocation density and partial recrystallisation inferred from Fig. 6d and d1. Vertically built specimens retain a pronounced deformation-controlled substructure (Fig. 7d1), in agreement with the persistent high-KAM bands and elongated grains observed in Fig. 6g and g1. ECCI confirms that the microstructural differences identified by EBSD and KAM are rooted in fundamentally different dislocation substructures and recovery–recrystallisation responses. While stress relief has a limited effect on the defect structure, solution annealing promotes significant dislocation annihilation and recrystallisation predominantly in horizontally built LPBF IN625.

3.2. Mechanical properties

The microstructural features described above, including grain morphology, crystallographic texture, dislocation substructure, and phase evolution, are expected to strongly influence the mechanical response of LPBF-fabricated IN625. These relationships are examined using tensile, hardness, and impact-toughness measurements.

Fig. 8 presents the tensile test results, including ultimate tensile strength (UTS), yield strength (YS), and elongation (EL), measured at

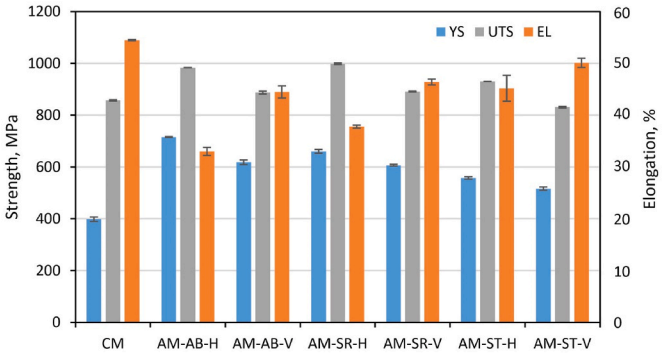

Fig. 8. Tensile properties: yield strength YS, ultimate tensile strength UTS and elongation EL of the investigated IN625 specimens.

room temperature for LPBF-fabricated IN625 specimens produced in both horizontal and vertical build orientations, in their as-built and heat-treated conditions. Results for the conventionally manufactured (wrought and solution-annealed) material are also included for comparison. A clear trend, also reported by other researchers [13,28] is observed: horizontally built specimens exhibit higher YS and, consequently, higher UTS than their vertically built counterparts. Conversely, vertically built specimens consistently show greater elongation, indicating superior ductility. This trend, being confirmed by ANOVA test as statistically significant (P-value $= 0.1 - 0.8 \times 10^{-3}$), persists across all processing states, whether in the as-built condition or following heat treatment.

These differences can be attributed to inherent characteristics of the LPBF process, with the observed anisotropy being strongly influenced by build orientation, which governs both grain morphology and crystallographic texture development. Horizontally built specimens tend to form larger, more equiaxed grains, which enhance strength (UTS and YS) but reduce ductility, likely due to grain boundary embrittlement and less compatible deformation. Vertically built specimens typically develop columnar grains aligned with the build direction, which support improved ductility through more compatible grain deformation and enhanced grain boundary migration.

These findings are consistent with those reported by Hu et al. [55] for IN625 produced by direct energy deposition (DED), further confirming the strong orientation-dependent mechanical behaviour characteristic of additively manufactured nickel-based superalloys.

Depending on the initial condition of the specimens, different tensile properties were observed, with the differences being identified as statistically significant (P-value $<2 \times 10^{-9}$). The highest ultimate tensile

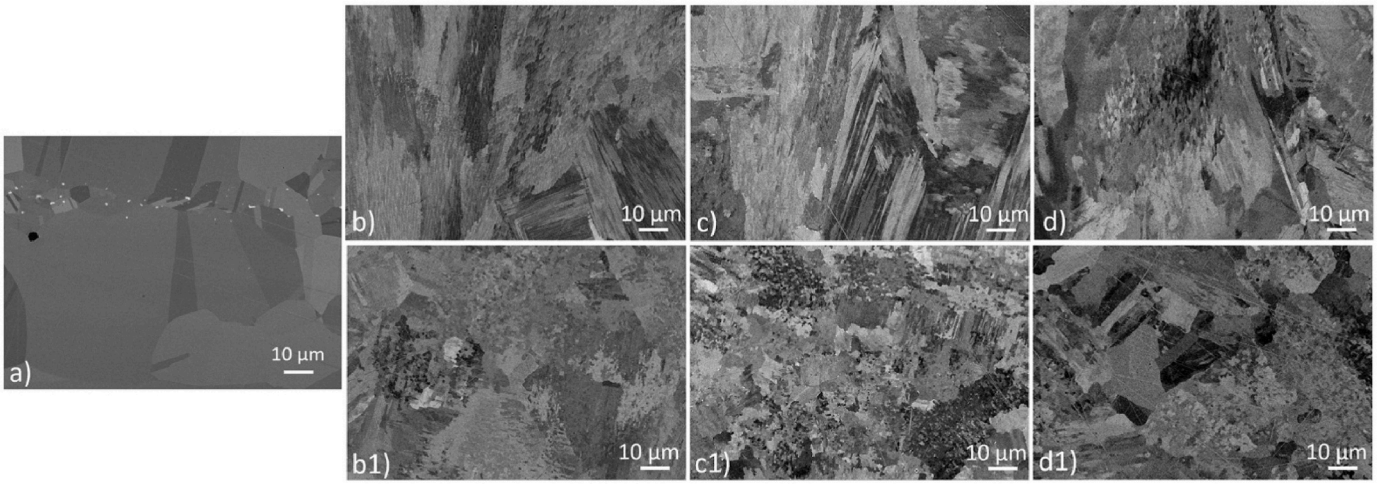

Fig. 7. ECCI images of IN625 specimens: (a) CM, (b) AM-AB-H, (c) AM-SR-H, (d) AM-ST-H, (b1) AM-AB-V, (c1) AM-SR-V, and (d1) AM-ST-V.

strength (UTS) was observed in the stress-relieved (SR) specimens, reaching 998 ± 3 MPa in the horizontal orientation and 891 ± 2 MPa in the vertical orientation. These were followed closely by the as-built specimens, with UTS values of 984 ± 1 MPa and 888 ± 6 MPa, respectively. This suggests that residual stresses introduced during the LPBF process may slightly reduce the tensile performance of the as-built condition. Specimens subjected to solution annealing (ST) exhibited lower UTS values, 931 ± 1 MPa (horizontal) and 831 ± 3 MPa (vertical), likely due to grain growth and the reduction in dislocation density following high-temperature treatment. The conventionally manufactured specimen exhibited the lowest UTS of 857 ± 2 MPa, consistent with its coarser grain structure and the absence of LPBF-induced microstructural refinement and strengthening mechanisms.

The highest yield strength (YS) was recorded for the as-built AM specimens, 715 ± 2 MPa in the horizontal and 618 ± 9 MPa in the vertical orientation. These values were followed by those of the SR specimens (660 ± 7 MPa and 606 ± 4 MPa, respectively), and then the ST specimens (557 ± 5 MPa and 516 ± 6 MPa). The lowest YS was again observed in the conventionally manufactured specimen, at 398 ± 9 MPa.

In terms of ductility, the as-built condition exhibited the lowest elongation values, 33.0 ± 0.8% for the horizontal and 44.6 ± 1.2% for the vertical orientation, reflecting the presence of high residual stresses and a highly anisotropic microstructure. The highest elongation was measured in the solution-annealed AM specimens (45.2 ± 2.5% and 50.1 ± 0.9%, respectively), due to the homogenised and recrystallised grain structure, which enables more uniform plastic deformation. The conventionally manufactured specimen exhibited the highest overall elongation at 54.5 ± 0.1%, consistent with its fully recrystallised, equiaxed microstructure.

Stress-relief annealing at 870 °C reduces residual stresses generated during LPBF without significantly altering the microstructure. As a result, UTS values show only a slight increase compared to the as-built state, while ductility improves marginally due to the relaxation of internal stresses. However, a more stable microstructure and less effective stress relief in the case of vertically built specimens is confirmed by smaller ductility improvement compared to the horizontal direction.

Solution annealing at 1050 °C leads to redissolution of segregation-induced phases and a reduction in both Laves phase content and dislocation density. Consequently, UTS and YS decrease relative to the as-built condition due to the loss of microsegregation-related strengthening. However, ductility improves significantly due to the more homogeneous, equiaxed microstructure, which facilitates enhanced plastic deformation.

Vickers hardness measurements (HV10) follow trends consistent with the tensile data and are presented in Fig. 9. The highest hardness is observed in the as-built condition (~309 ± 7 HV10 for both build orientations), attributed to the high cooling rates and rapid solidification inherent to the LPBF process. Hardness values in the as-built state are known to depend on specific process parameters, with the literature reporting typical values in the range of ~20–30 HRC [20,56], which correlate with the corresponding HV10 measurements. Following stress-relief annealing, the hardness decreases slightly (288 ± 2 HV10) and reaches its lowest value after solution annealing (~250 ± 2 HV10). Despite this reduction, LPBF-fabricated IN625 retains a higher hardness than conventionally processed IN625 subjected to the same heat treatment. This is primarily due to its finer recrystallised grain structure, which enhances hardness even after homogenization.

The observed decrease in hardness with increasing heat-treatment temperature is consistent with a well-documented trend in LPBF-processed IN625 alloys [57]. This behaviour is primarily attributed to the dissolution of the fine cellular or dendritic substructure, the recovery of internal stresses, and grain growth, all of which reduce the microstructural strengthening mechanisms present in the as-built condition. The limited influence of build orientation on hardness indicates that hardness is primarily governed by local microstructural features, such as dislocation density and substructure, rather than by macroscopic grain morphology. A small difference in hardness between the horizontally and vertically built specimens (~1%) is observed only after solution annealing. This difference arises from the more extensive recrystallisation occurring in the horizontally built specimens compared to the vertically built ones (Fig. 6d and g).

Impact toughness, measured using the standard Charpy V-notch (CVN) test, is a critical property for IN625, particularly for high-temperature applications. Fig. 10 summarises the impact toughness of conventionally manufactured (CM) and LPBF-produced IN625 specimens tested at room temperature (RT) and at a specimen temperature of 650 °C, 750 °C, and 850 °C, highlighting the effects of manufacturing route, build orientation, heat treatment, and test temperature. Similar to tensile properties, results show statistically significant difference between vertical and horizontal build directions (P-value $<9 \times 10^{-3}$) as well as depending on the heat treatment condition (P-value $<1 \times 10^{-6}$).

At room temperature, the conventionally manufactured and solution-annealed material exhibits the highest impact toughness (149.4 ± 2 J). This behaviour is consistent with its fully recrystallised, equiaxed, and homogenised microstructure, characterised by low lattice curvature and dislocation density, as confirmed by EBSD/KAM analysis. The combination of high ductility and relatively high flow stress at RT enables extensive plastic deformation ahead of the notch, resulting in high absorbed energy during impact loading.

All LPBF specimens exhibit reduced impact toughness compared to the CM material, reflecting processing-induced anisotropy and microstructural heterogeneity. A clear build-orientation dependence is observed, with vertically built specimens consistently exhibiting higher impact toughness than horizontally built ones. This difference is attributed to the interaction between crack propagation and the layer-wise LPBF microstructure. In vertically built specimens, the crack front intersects pronounced columnar grains, increasing crack-path tortuosity and energy dissipation. Horizontally built specimens favour

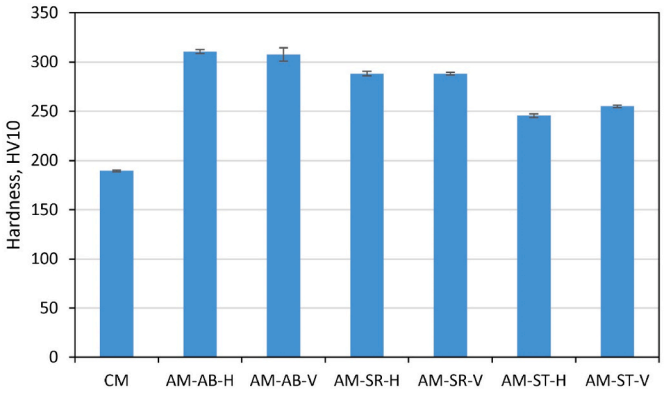

Fig. 9. Vickers hardness HV10 of the investigated IN625 specimens.

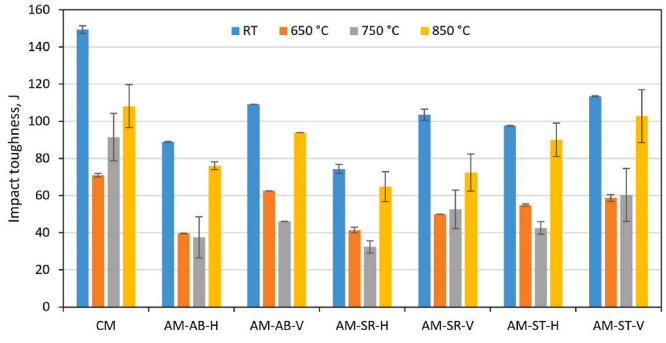

Fig. 10. Charpy impact toughness at room temperature (RT) and at elevated temperatures (650 °C, 750 °C and 850 °C) of the investigated IN625 specimens.

crack propagation along melt-pool and grain boundaries, which act as preferential fracture paths and reduce absorbed energy. In the as-built condition, this results in impact toughness values of 109.1 ± 0.9 J for vertically built and 88.9 ± 0.2 J for horizontally built specimens.

Stress-relief annealing at 870 °C for 1 h produces only minor changes in impact toughness. Although residual stresses are reduced through recovery, the columnar grain structure and cellular substructure are largely preserved, limiting improvements in fracture resistance. The slight reduction in impact toughness after stress-relief annealing, particularly in horizontally built specimens, can be attributed to δ-phase (Ni_3Nb) precipitation along former cell boundaries combined with dislocation rearrangement [39]. While recovery reduces residual stresses, it may also decrease strain hardening capacity and promote earlier crack initiation.

Solution annealing at 1050 °C for 1 h leads to partial recrystallisation and microstructural homogenization, reducing anisotropy and internal stress concentrations. Consequently, impact toughness increases to 113.4 ± 0.3 J for vertically built and a bit more effectively to 97.6 ± 0.2 J for horizontally built LPBF specimens, although these values remain below those of the CM material due to incomplete recrystallisation and persistent microstructural inheritance from the LPBF process.

Testing at elevated temperatures reveals a pronounced minimum in impact toughness between 650 °C and 750 °C for all specimen conditions, followed by a recovery above 750 °C and the highest elevated-temperature toughness at 850 °C. The reduction and increased scattering of results between 650 °C and 750 °C are attributed to unstable, localised deformation at the notch root, commonly associated with dynamic strain-ageing-type behaviour in IN625 under high-strain-rate loading. In this temperature range, interactions between diffusing solute atoms and moving dislocations promote strain localisation and reduce the stability of the plastic zone, accelerating crack initiation despite the increased temperature. As the test temperature increases above 750 °C, thermally activated dislocation mechanisms such as cross-slip, climb, and dynamic recovery become more effective, leading to more homogeneous viscoplastic deformation and enhanced crack-tip blunting. As a result, impact toughness increases with temperature beyond 750 °C.

Post-processing heat treatments significantly affect the impact toughness of LPBF IN625 at elevated temperatures, with stress relieving reducing and solution annealing enhancing high-temperature toughness. However, the influence of building orientation remains evident, with vertical building direction being superior, thus underscoring the critical role of processing-induced anisotropy in governing impact fracture behaviour.

Fig. 11 shows SEM micrographs of fracture surfaces of Charpy V-notch specimens tested at room temperature for conventionally manufactured and LPBF IN625 in different build orientations and heat-treatment conditions. All specimens exhibit predominantly ductile fracture characterised by microvoid coalescence, consistent with the high impact toughness measured at room temperature. Differences in fracture morphology are primarily associated with the manufacturing route and heat-treatment condition, while orientation-related effects are less pronounced at this magnification.

The conventionally manufactured specimen (CM) exhibits large, deep, and uniformly distributed dimples, indicative of extensive plastic deformation prior to fracture. This fracture morphology correlates with the highest absorbed impact energy and with EBSD/KAM results showing a fully recrystallised, equiaxed microstructure with very low lattice curvature and dislocation density.

LPBF specimens generally display finer and less uniform dimples, reflecting the influence of the layer-wise microstructure and higher local lattice curvature. In the as-built and stress-relieved conditions, locally shallow dimples and occasional planar regions are observed, consistent with deformation localisation and similar impact toughness values after stress-relief annealing. These features agree with δ phase precipitation, EBSD evidence of recovery without recrystallisation and persistently elevated KAM values.

After solution annealing, LPBF specimens exhibit more homogeneous fracture surfaces with more uniformly distributed dimples, indicating enhanced plastic deformation and correlating with reduced lattice curvature and partial recrystallisation observed by EBSD/KAM. At room temperature, no pronounced differences in dimple morphology are observed between horizontally and vertically built solution-annealed specimens, suggesting that orientation-dependent differences in impact toughness are not governed by the final microvoid coalescence mechanism but rather by crack initiation and propagation processes on larger length scales.

Overall, the fracture surface analysis at room temperature supports the Charpy impact results and EBSD observations, confirming that higher impact toughness is associated with a more homogeneous ductile fracture response and reduced lattice curvature, whereas lower toughness correlates with localised deformation and inherited LPBF microstructural features.

Mechanical testing confirms that both build orientation and post-processing heat treatments significantly impact the performance of LPBF-fabricated IN625 alloy. The pronounced anisotropy observed in

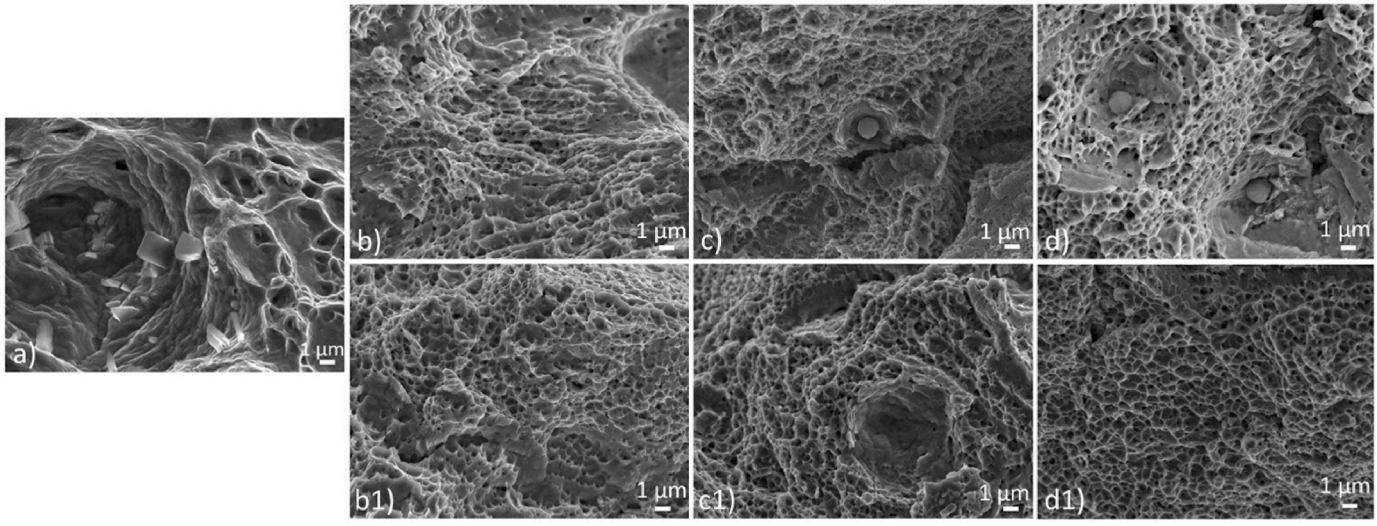

Fig. 11. SEM micrograph of the fracture surface for CVN test specimens of IN625: (a) CM, (b) AM-AB-H, (c) AM-SR-H, (d) AM-ST-H, (b1) AM-AB-V, (c1) AM-SR-V, and (d1) AM-ST-V.

mechanical properties is primarily attributed to build-orientation-dependent microstructural features, including variations in grain morphology and grain boundary characteristics. Investigated post-processing treatments (stress-relief and solution annealing) were found effective in reducing residual stresses and promoting microstructural homogenization. These treatments help mitigate anisotropy and enhance the material's overall mechanical performance.

3.3. Wear resistance

Results of wear testing are shown in Fig. 12, with the corresponding wear scar width and depth provided in Table 4 and coefficient of friction curves in Fig. 13. In the case of conventional, solution annealed IN625 steady-state coefficient of friction against hardened bearing steel ball is at the level of 0.630 ± 0.001, indicating abrasive wear as the prevailing wear mechanism, combined with wear particles oxidation and adhesion, which was further confirmed by wear scar analysis (Fig. 14a). Wear volume after 5 m of dry sliding at room temperature was 0.0143 ± 0.0004 mm^3, corresponding to a wear rate of 1.43 × 10^{-4} mm^3/Nm. As-built LPBF specimens show slightly lower steady-state friction (0.58 ± 0.02) without any noticeable effect of build and/or sliding direction. However, in the case of LPBF IN625 with higher hardness and strength abrasive wear component with wear particles generation and oxidation became more pronounced (Fig. 14b). Consequently, for horizontal building direction and sliding across layers (⊥) wear volume of as-build IN625 increased to 0.0186 ± 0.0016 mm^3 and for sliding along layers (=) even to 0.0271 ± 0.0001 mm^3 (Fig. 12a). Similar trend was observed for vertically build specimens, however, those showing lower wear (~0.015 ± 0.002 mm^3), comparable to conventional IN625, and smaller difference between perpendicular and parallel sliding direction. Increased wear, especially for horizontal build direction is related to reduced toughness and ductility, thus promoting more brittle material behaviour with a higher wear particles generation rate. On the other hand, lower wear for vertically built specimens as compared to horizontal ones can be ascribed to microstructure of longer and more continuous columnar grains, as well as higher density of dislocations, which more effectively hinder crack propagation and wear process. This effect is further emphasised for parallel sliding direction (=), perpendicular to the grain orientation.

With heat treatment, the difference between horizontally and vertically built specimens largely disappeared, being related to microstructure recovery, homogenization and recrystallisation. After stress-relief annealing at 870 °C dislocations rearrangement and residual stress relaxation had no effect on wear mechanism and friction level (0.59 ± 0.02) but led to reduced wear volume (~0.011 ± 0.001 mm^3), with vertically built specimens still showing about 10% better wear resistance. However, recrystallisation of LPBF IN625 specimens obtained by solution annealing at 1050 °C promoted adhesion of steel counter-material (Fig. 14c), with the coefficient of friction consequently increasing to 0.75 ± 0.02 (Fig. 12b) and wear volume and wear rate reaching minimum of 0.0085 ± 0.0004 mm^3 and 0.85 × 10^{-4} mm^3/Nm, respectively (Fig. 12a). Better wear resistance of solution annealed LPBF IN625 specimens as compared to conventional IN625 is statistically significant (*P*-value <1 × 10^{-4}) and consistent with their finer microstructure and higher hardness.

Table 4
Wear scar width and depth data.

Specimen	Perpendicular sliding (⊥)		Parallel sliding (=)	
	Width (mm)	Depth (μm)	Width (mm)	Depth (μm)
CM	0.956 ± 0.013	7.10 ± 0.01	/	/
AM-AB-H	1.691 ± 0.053	8.47 ± 0.03	1.645 ± 0.049	10.89 ± 0.01
AM-AB-V	1.468 ± 0.095	7.00 ± 0.03	1.450 ± 0.018	7.93 ± 1.02
AM-SR-H	0.917 ± 0.027	6.22 ± 0.02	0.906 ± 0.101	5.82 ± 0.28
AM-SR-V	0.905 ± 0.039	6.04 ± 0.02	0.840 ± 0.067	5.42 ± 0.15
AM-ST-H	0.872 ± 0.059	5.46 ± 0.01	0.844 ± 0.039	4.83 ± 0.08
AM-ST-V	0.850 ± 0.020	5.05 ± 0.01	0.885 ± 0.008	5.19 ± 0.58

3.4. Corrosion resistance

The corrosion performance of the investigated specimens was evaluated using potentiodynamic polarisation measurements (Fig. 15). The corresponding corrosion potentials (E_{corr}), corrosion current densities (i_{corr}), and corrosion rates (v_{corr}) are summarised in Table 5. The values of i_{corr} and v_{corr} were calculated in accordance with ASTM G102-89:2015 [58]. Standard deviations are consistently low across all the investigated specimens, indicating good reproducibility of the measurements. The highest corrosion rates were observed in the as-built specimens, regardless of build orientation. It was initially expected that horizontally built specimens might exhibit slightly higher corrosion rates due to a greater likelihood of surface defects acting as pitting initiation sites. However, all specimens were diamond-polished prior to testing, thereby eliminating the influence of surface roughness and defect-related effects between orientations. The lower corrosion resistance of the as-built condition can be attributed to its anisotropic microstructure, characterised by a fine cellular or dendritic substructure aligned with the build direction, and by the microsegregation of Nb and Mo into Laves phase. These features are known to reduce corrosion resistance in chloride-containing environments, as compared to the more homogeneous microstructure of wrought material [59].

Heat-treated specimens exhibited improved corrosion resistance relative to the as-built condition. Stress-relief annealing at 870 °C reduced residual stresses generated during the LPBF process but did not significantly alter the underlying microstructure. As a result, the corrosion behaviour remained influenced by the presence of the Laves phase and compositional heterogeneity. Due to the uniform surface finish applied to all specimens, corrosion rates for horizontally and vertically built stress-relieved specimens were comparable. Specimens subjected to solution annealing demonstrated the highest corrosion resistance, approaching that of conventionally manufactured material. The heat treatment at 1050 °C eliminated the dendritic structure, promoted the dissolution of segregation-induced phases such as Laves phase, and facilitated the redistribution of Nb and Mo within the γ

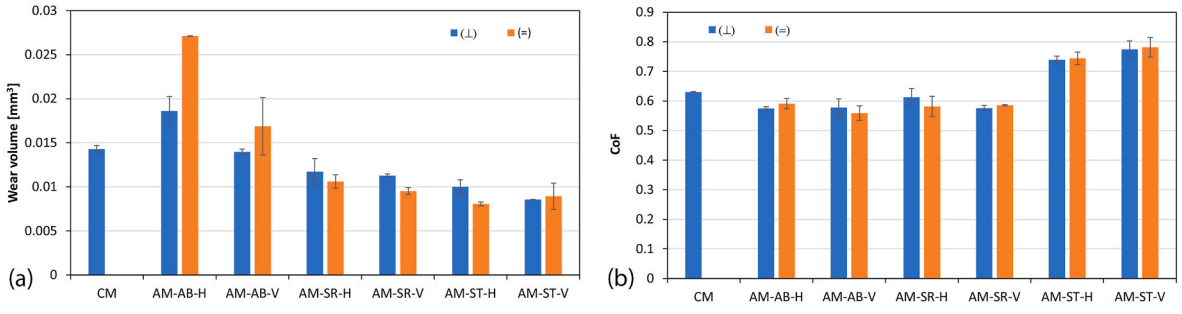

Fig. 12. Wear test results for the investigated IN625 specimens: (a) wear volume and (b) steady-state coefficient of friction.

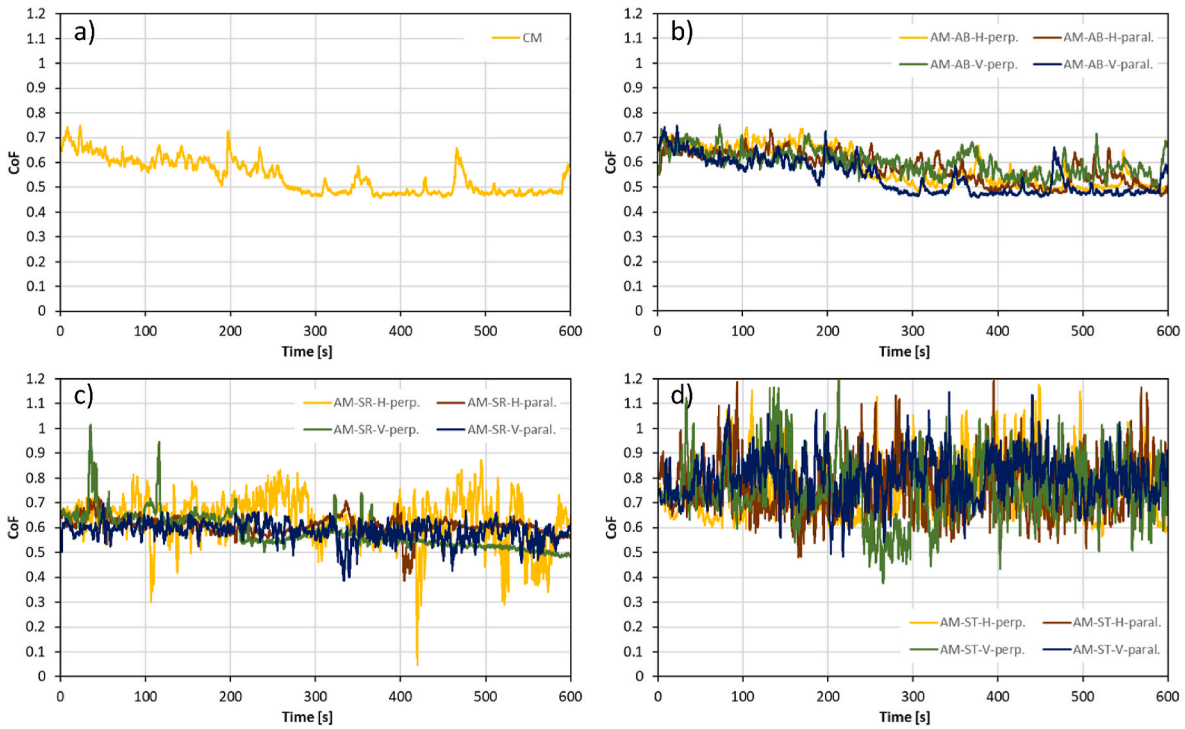

Fig. 13. Coefficient of friction curves for the investigated IN625 specimens: (a) CM, AM-AB, (c) AM-SR and (d) AM-ST.

matrix. This resulted in enhanced chemical homogeneity, which plays a key role in improving corrosion performance [60]. Reduced microsegregation limits the formation of local galvanic couples, while a more uniform distribution of alloying elements promotes the development of a more stable and protective passive film. Together with recrystallisation and grain growth, these microstructural changes reduce corrosion current density and improve overall corrosion resistance.

The corrosion behaviour of LPBF IN625 is therefore governed by microstructural heterogeneity and elemental segregation, which promote localised corrosion in chloride-containing environments [61]. Solution annealing improves corrosion resistance by dissolving segregation-induced phases and homogenising the microstructure, thereby reducing microgalvanic interactions and enhancing passive film stability [62].

4. Conclusions

This study investigates the effects of build orientation and post-processing heat treatments on mechanical performance, including impact toughness at both room and elevated temperatures, as well as tribological and corrosion behaviour. The study has resulted in the following conclusions:

- The as-built LPBF IN625 exhibits a highly anisotropic microstructure characterised by elongated columnar grains, a fine cellular/dendritic substructure, and a high density of dislocations. These features are strongly dependent on build orientation. Vertically built specimens exhibit greater continuity of columnar grains and increased local lattice curvature compared to horizontally built ones. EBSD/KAM and ECCI analyses demonstrate that this inherited LPBF microstructure governs the anisotropic mechanical response of the material.
- Stress-relief annealing at 870 °C effectively reduces residual stresses through recovery but does not fundamentally alter the solidification-induced microstructure. Grain morphology, texture, and dislocation substructure remain largely unchanged, and recrystallisation is not observed. Consequently, mechanical anisotropy persists, limiting improvements in ductility, hardness and impact toughness. The treatment promotes the precipitation of Nb-rich secondary phases, primarily δ phase, particularly in vertically built specimens due to enhanced microsegregation.
- Solution annealing at 1050 °C induces significant microstructural homogenization through the dissolution of segregation-induced phases and partial recrystallisation. The extent of recrystallisation is strongly orientation dependent. Horizontally built specimens undergo more extensive recrystallisation, leading to a reduction in dislocation density, lower lattice curvature, and a more equiaxed grain structure. Vertically built specimens retain portions of the columnar architecture and deformation-controlled substructure, indicating a lower effective driving force for recrystallisation.
- Microstructural differences directly translate into mechanical behaviour. Horizontally built specimens consistently exhibit higher yield and tensile strengths, whereas vertically built specimens show superior ductility and impact toughness. Hardness decreases with increasing heat-treatment temperature due to recovery, recrystallisation, and grain growth. A clear orientation-dependent difference is observed only after solution annealing, indicating that recrystallisation is more advanced in horizontally built material.
- Corrosion resistance is strongly governed by microstructural homogeneity. As-built specimens exhibit the lowest corrosion resistance due to microsegregation and the presence of segregation-related phases. Stress-relief annealing yields moderate improvement, while solution annealing significantly enhances corrosion resistance by eliminating the dendritic substructure and redistributing Nb and Mo within the γ matrix. After solution annealing, the corrosion performance of LPBF specimens approaches that of conventionally manufactured IN625.
- Although as-built LPBF IN625 displays higher hardness and strength than conventional IN625, its greater brittleness results in a combination of adhesive and abrasive wear, leading to increased total wear rate. However, pronounced columnar grain microstructure and a higher dislocation density make the vertically built material more wear-resistant, especially under sliding parallel to the building layers. Differences in wear behaviour between horizontal and

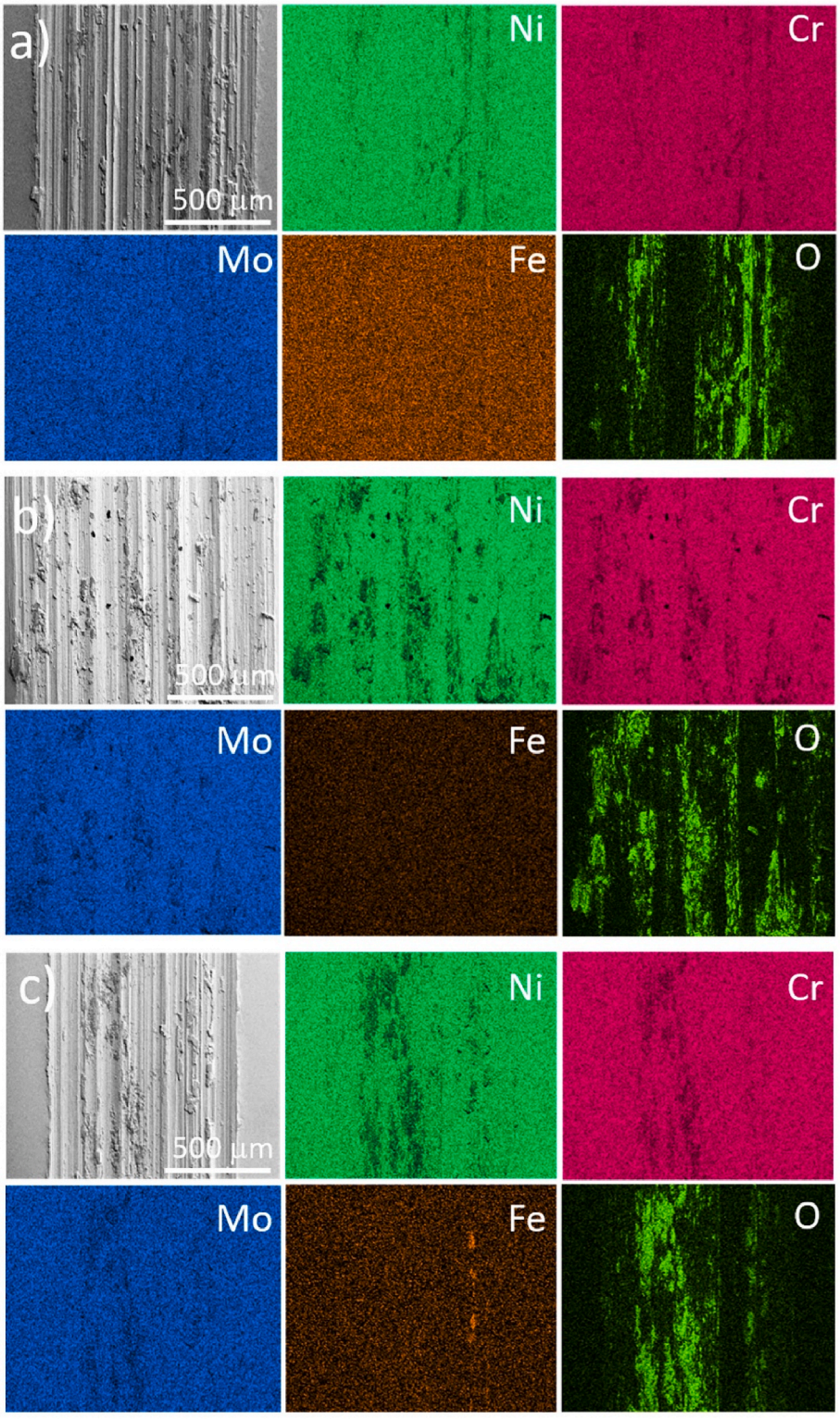

Fig. 14. Wear scar SEM micrographs with corresponding EDS maps for the specimens: (a) CM, (b) AM-AB-H (⊥ sliding direction) and (c) AM-ST-H (⊥ sliding direction).

vertical building directions diminish after heat-treatment. Stress-relieving and microstructure recovery result in a maintained friction level and reduced wear, while solution annealing with microstructure homogenization and recrystallisation provide superior wear resistance but high friction.

The results demonstrate that LPBF Inconel 625 does not respond uniformly to conventional heat-treatment protocols and that build orientation plays a decisive role in controlling microstructural stability, recrystallisation kinetics, and property anisotropy. While stress-relief treatment primarily alleviates residual stresses, high-temperature solution annealing is required to substantially homogenise the microstructure and mitigate LPBF-induced anisotropy. These findings provide important guidelines for tailoring post-processing strategies to achieve

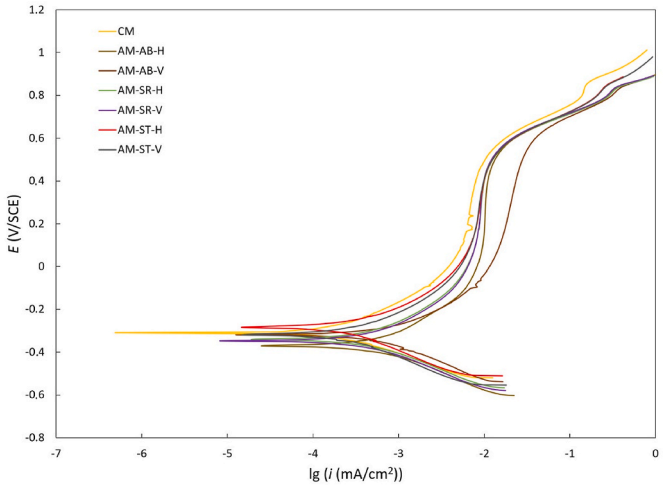

Fig. 15. Potentiodynamic curves for the investigated IN625 specimens in 3.5% NaCl solution.

Table 5
Electrochemical parameters determined from the potentiodynamic curves.

Specimen	E_{corr} (mV)	i_{corr} (μA/cm^2)	v_{corr} (μm/year)
CM	−308 ± 1	0.23 ± 0.01	2.3 ± 0.1
AM-AB-H	−369 ± 2	0.88 ± 0.03	8.7 ± 0.3
AM-AB-V	−318 ± 1	0.87 ± 0.03	8.6 ± 0.3
AM-SR-H	−339 ± 3	0.60 ± 0.02	6.0 ± 0.2
AM-SR-V	−346 ± 4	0.60 ± 0.02	5.9 ± 0.2
AM-ST-H	−282 ± 1	0.38 ± 0.01	3.8 ± 0.1
AM-ST-V	−317 ± 1	0.36 ± 0.01	3.6 ± 0.1

application-specific combinations of strength, ductility, toughness, and corrosion resistance in LPBF-fabricated IN625 components.

Declaration of generative AI and AI-assisted technologies in the manuscript preparation process

During the preparation of this work the authors used ChatGPT (version 5.2) in order to improve the English language and enhance the clarity, coherence, and overall readability of the text. After using this tool, the authors reviewed and edited the content as needed and take full responsibility for the content of the published article.

CRediT authorship contribution statement

Danijela A. Skobir Balantič: Conceptualization, Investigation, Writing - Original draft preparation, Writing - Review & Editing, Data Curation. Črtomir Donik: Investigation, Writing - Review & Editing. Bojan Podgornik: Investigation, Writing - Original draft preparation, Writing - Review & Editing. Aleksandra Kocijan: Investigation, Writing - Original draft preparation, Writing - Review & Editing. Matjaž Godec: Conceptualization, Investigation, Writing - Original draft preparation, Writing - Review & Editing, Supervision.

Declaration of competing interest

The authors declare that they have no known competing financial interests or personal relationships that could have appeared to influence the work reported in this paper.

Acknowledgments

The authors acknowledge the financial support from the Slovenian Research and Innovation Agency (research core funding Nos. P2-0132 and P2-0050 and Infrastructure Programme I0-0006).

Data availability

The data [63] supporting the findings of this study are available in the Zenodo repository at: https://doi.org/10.5281/zenodo.18605408.

References

[1] Shoemaker LE. Alloys 625 and 725: trends in properties and applications. In: Superalloys 718, 625, 706 and Various Derivatives. TMS; 2005. p. 409–18. https://doi.org/10.7449/2005/Superalloys_2005_409_418. 2005.
[2] Zhang F, Levine LE, Allen AJ, Stoudt MR, Lindwall G, Lass EA, Williams ME, Idell Y, Campbell CE. Effect of heat treatment on the microstructural evolution of a nickel-based superalloy additive-manufactured by laser powder bed fusion. Acta Mater 2018;152:200–14. https://doi.org/10.1016/j.actamat.2018.03.017.
[3] Paul CP, Ganesh P, Mishra SK, Bhargava P, Negi J, Nath AK. Investigating laser rapid manufacturing for Inconel-625 components. Opt Laser Technol 2007;39:800–5. https://doi.org/10.1016/j.optlastec.2006.01.008.
[4] Li C, White R, Fang XY, Weaver M, Guo YB. Microstructure evolution characteristics of Inconel 625 alloy from selective laser melting to heat treatment. Mater Sci Eng, A 2017;705:20–31. https://doi.org/10.1016/j.msea.2017.08.058.
[5] Li D, Guo Q, Guo S, Peng H, Wu Z. The microstructure evolution and nucleation mechanisms of dynamic recrystallization in hot-deformed Inconel 625 superalloy. Mater Des 2011;32:696–705. https://doi.org/10.1016/j.matdes.2010.07.040.
[6] Günen A, Gürol U, Çakan A, Koçak M, Çam G, Yildizhan H, Alsaadi A, Gomes J. Effect of post-deposition aluminizing on the corrosion and mechanical behavior of WAAM-fabricated stainless steel and Ni-based superalloy. Sci Rep 2025;15:43268. https://doi.org/10.1038/s41598-025-30389-4.
[7] Ceritbinmez F, Günen A, Gürol U, Çam G. A comparative study on drillability of Inconel 625 alloy fabricated by wire arc additive manufacturing. J Manuf Process 2023;89:150–69. https://doi.org/10.1016/j.jmapro.2023.01.072.
[8] Gonzalez JA, Mireles J, Stafford SW, Perez MA, Terrazas CA, Wicker RB. Characterization of Inconel 625 fabricated using powder-bed-based additive manufacturing technologies. J Mater Process Technol 2019;264:200–10. https://doi.org/10.1016/j.jmatprotec.2018.08.031.
[9] Marchese G, Lorusso M, Parizia S, Bassini E, Lee J-W, Calignano F, Manfredi D, Terner M, Hong H-U, Ugues D, Lombardi M, Biamino S. Influence of heat treatments on microstructure evolution and mechanical properties of Inconel 625 processed by laser powder bed fusion. Mater Sci Eng, A 2018;729:64–75. https://doi.org/10.1016/j.msea.2018.05.044.
[10] Badea TA, Condruz MR. Investigation on improving the hot corrosion resistance of selective laser melting manufactured inconel 625 by pre-oxidation heat treatment. Materials 2025;18:1111. https://doi.org/10.3390/ma18051111.
[11] Karakas MS, Günen A, Lindner T, Küçük Y, Kon Ö, Joshi S, Çam G, Lampke T. Comparative study of heat treatment routes for enhancing high-temperature wear resistance of EBM-processed Inconel 718. Mater Today Commun 2025;49:113864. https://doi.org/10.1016/j.mtcomm.2025.113864.
[12] Günen A, Heidarzadeh A, Ceritbinmez F, Kanca E, Li W, Çam G. Drilling response of additively manufactured and cast AISI H13 hot-work tool steel by thermal and mechanical processes. Progr Addit Manuf 2026;11:157–79. https://doi.org/10.1007/s40964-025-01340-w.
[13] Liu J, Zhou L, Peng Z, Chen B, Tan Y, Chen J, Huang W, Li C. Anisotropy evolution of tensile properties in laser powder bed fusion-fabricated inconel 625 alloy at high temperature. Acta Metall Sin 2025;38:555–69. https://doi.org/10.1007/s40195-025-01828-y.
[14] Rodrigues Da Silva J, Hamouche Z, Helbert AL, Baudin T, Coste F, Peyre P. Influence of diameter and scan strategy on the geometrical, microstructural, and mechanical properties of small Inconel 625 L-PBF struts. J Mater Process Technol 2025;336. https://doi.org/10.1016/j.jmatprotec.2024.118702.
[15] Mostafaei A, Ghiaasiaan R, Ho I-T, Strayer S, Chang K-C, Shamsaei N, Shao S, Paul S, Yeh A-C, Tin S, To AC. Additive manufacturing of nickel-based superalloys: a state-of-the-art review on process-structure-defect-property relationship. Prog Mater Sci 2023;136:101108. https://doi.org/10.1016/j.pmatsci.2023.101108.
[16] Herzog D, Seyda V, Wycisk E, Emmelmann C. Additive manufacturing of metals. Acta Mater 2016;117:371–92. https://doi.org/10.1016/j.actamat.2016.07.019.
[17] Zhu J, Shao C, Lu F, Feng K, Liu P, Chu S, Feng Y, Kokawa H, Li Z. Origin of the anisotropic ductility and the dynamic recrystallization-like deformation behavior of laser powder bed fusion Inconel 625 at elevated temperature. Scr Mater 2022;221:114945. https://doi.org/10.1016/j.scriptamat.2022.114945.
[18] Hu YL, Lin X, Lu XF, Zhang SY, Yang HO, Wei L, Huang WD. Evolution of solidification microstructure and dynamic recrystallisation of Inconel 625 during laser solid forming process. J Mater Sci 2018;53:15650–66. https://doi.org/10.1007/s10853-018-2701-x.
[19] Benoit MJ, Mazur M, Easton MA, Brandt M. Effect of alloy composition and laser powder bed fusion parameters on the defect formation and mechanical properties of Inconel 625. Int J Adv Manuf Technol 2021;114:915–27. https://doi.org/10.1007/s00170-021-06957-z.
[20] Diaz JC, Watanabe K, Rubio A, De La Cruz A, Godinez D, Nabil ST, Murr LE, Wicker RB, Arrieta E, Medina F. Effect of layer thickness and heat treatment on microstructure and mechanical properties of alloy 625 manufactured by electron beam powder bed fusion. Materials 2022;15:7767. https://doi.org/10.3390/ma15217767.

[21] Marchese G, Garmendia Colera X, Calignano F, Lorusso M, Biamino S, Minetola P, Manfredi D. Characterization and comparison of inconel 625 processed by selective laser melting and laser metal deposition. Adv Eng Mater 2017;19. https://doi.org/10.1002/adem.201600635.
[22] Yadroitsev I, Thivillon L, Bertrand Ph, Smurov I. Strategy of manufacturing components with designed internal structure by selective laser melting of metallic powder. Appl Surf Sci 2007;254:980–3. https://doi.org/10.1016/j.apsusc.2007.08.046.
[23] Kocaman E, Gürol U, Günen A, Çam G. Effect of post-deposition heat treatments on high-temperature wear and corrosion behavior of Inconel 625. Mater Today Commun 2025;42:111101. https://doi.org/10.1016/j.mtcomm.2024.111101.
[24] Gürol U, Altınay Y, Günen A, Bölükbaşı ÖS, Koçak M, Çam G. Effect of powder-pack aluminizing on microstructure and oxidation resistance of wire arc additively manufactured stainless steels. Surf Coat Technol 2023;468:129742. https://doi.org/10.1016/j.surfcoat.2023.129742.
[25] Li S, Wei Q, Shi Y, Zhu Z, Zhang D. Microstructure characteristics of inconel 625 superalloy manufactured by selective laser melting. J Mater Sci Technol 2015;31:946–52. https://doi.org/10.1016/j.jmst.2014.09.020.
[26] Brown CU, Jacob G, Stoudt M, Moylan S, Slotwinski J, Donmez A. Interlaboratory study for nickel alloy 625 made by laser powder bed fusion to quantify mechanical property variability. J Mater Eng Perform 2016;25:3390–7. https://doi.org/10.1007/s11665-016-2169-2.
[27] Yan X, Gao S, Chang C, Huang J, Khanlari K, Dong D, Ma W, Fenineche N, Liao H, Liu M. Effect of building directions on the surface roughness, microstructure, and tribological properties of selective laser melted Inconel 625. J Mater Process Technol 2021;288:116878. https://doi.org/10.1016/j.jmatprotec.2020.116878.
[28] Poulin J-R, Brailovski V, Terriault P. Long fatigue crack propagation behavior of Inconel 625 processed by laser powder bed fusion: influence of build orientation and post-processing conditions. Int J Fatig 2018;116:634–47. https://doi.org/10.1016/j.ijfatigue.2018.07.008.
[29] Heo S, Lim Y, Kwak N, Jeon C, Choi M, Jo I. Impact of heat treatment and building direction on tensile properties and fracture mechanism of inconel 718 produced by SLM process. Metals 2024;14:440. https://doi.org/10.3390/met14040440.
[30] Du D, Dong A, Shu D, Zhu G, Sun B, Li X, Lavernia E. Influence of build orientation on microstructure, mechanical and corrosion behavior of Inconel 718 processed by selective laser melting. Mater Sci Eng, A 2019;760:469–80. https://doi.org/10.1016/j.msea.2019.05.013.
[31] Jeyaprakash N, Yang C-H, Prabu G, Clinktan R. Microstructure and tribological behaviour of Inconel-625 superalloy produced by selective laser melting. Met Mater Int 2022;28:2997–3015. https://doi.org/10.1007/s12540-022-01198-5.
[32] Ferraresi R, Avanzini A, Cecchel S, Petrogalli C, Cornacchia G. Microstructural, mechanical, and tribological evolution under different heat treatment conditions of inconel 625 alloy fabricated by selective laser melting. Adv Eng Mater 2022;24. https://doi.org/10.1002/adem.202100966.
[33] Zhu J, Kokawa H, Feng K, Li Z. Unexpectedly high corrosion susceptibility near fusion boundaries of Inconel 625 manufactured by laser powder bed fusion. Corros Sci 2023;223:111432. https://doi.org/10.1016/j.corsci.2023.111432.
[34] DIN 50125:2022-08, Prüfung Metallischer Werkstoffe_- Zugproben. 2022. https://doi.org/10.31030/3337825.
[35] International Organization for Standardization, Metallic Materials — Tensile Testing — Part 1: Method of Test at Room Temperature, ISO 6892-1:2019, Geneva, Switzerland, 2019, (n.d.).
[36] International Organization for Standardization. Metallic Materials — Charpy Pendulum Impact Test — Part 1: Test Method, ISO 148-1:2016, Geneva, Switzerland. 2016. n.d.
[37] Nguejio J, Szmytka F, Hallais S, Tanguy A, Nardone S, Godino Martinez M. Comparison of microstructure features and mechanical properties for additive manufactured and wrought nickel alloys 625. Mater Sci Eng, A 2019;764:138214. https://doi.org/10.1016/j.msea.2019.138214.
[38] Mohammadpour P, Yuan H, Phillion AB. Microstructure evolution of Inconel 625 alloy during single-track laser powder bed fusion. Addit Manuf 2022;55:102824. https://doi.org/10.1016/j.addma.2022.102824.
[39] Lass EA, Stoudt MR, Williams ME, Katz MB, Levine LE, Phan TQ, Gnaeupel-Herold TH, Ng DS. Formation of the Ni3Nb δ-Phase in stress-relieved inconel 625 produced via laser powder-bed fusion additive manufacturing. Metall Mater Trans 2017;48:5547–58. https://doi.org/10.1007/s11661-017-4304-6.
[40] Stoudt MR, Lass EA, Ng DS, Williams ME, Zhang F, Campbell CE, Lindwall G, Levine LE. The influence of annealing temperature and time on the formation of δ-Phase in additively-manufactured inconel 625. Metall Mater Trans 2018;49:3028–37. https://doi.org/10.1007/s11661-018-4643-y.
[41] Zhu J, Feng K, Kokawa H, Li Z. Effect of heat treatment on the anisotropic mechanical properties and corrosion resistance of laser powder bed fusion fabricated Inconel 625. J Alloys Compd 2024;1001:175087. https://doi.org/10.1016/j.jallcom.2024.175087.
[42] Lass EA, Stoudt MR, Katz MB, Williams ME. Precipitation and dissolution of δ and γ″ during heat treatment of a laser powder-bed fusion produced Ni-based superalloy. Scr Mater 2018;154:83–6. https://doi.org/10.1016/j.scriptamat.2018.05.025.
[43] Staroń S, Macioł P, Dubiel B, Gola K, Falkus J. Evolution of δ phase precipitates in Inconel 625 superalloy additively manufactured by laser powder bed fusion and its modeling with fuzzy logic. Arch Civ Mech Eng 2023;23:86. https://doi.org/10.1007/s43452-023-00626-6.
[44] Yang F, Dong L, Hu X, Zhou X, Xie Z, Fang F. Effect of solution treatment temperature upon the microstructure and mechanical properties of hot rolled Inconel 625 alloy. J Mater Sci 2020;55:5613–26. https://doi.org/10.1007/s10853-020-04375-2.
[45] Zhang F, Ilavsky J, Lindwall G, Stoudt MR, Levine LE, Allen AJ. Solid-state transformation of an additive manufactured Inconel 625 alloy at 700 °C. Appl Sci 2021;11:8643. https://doi.org/10.3390/app11188643.
[46] Lourenço JC, Souza LP, Faria MIST, Nunes CA, Tomachuk CR, Baker MA. Influence of the iron content on the microstructure and electrochemical behavior of as-cast modified Inconel 625. Corros Sci 2021;193:109892. https://doi.org/10.1016/j.corsci.2021.109892.
[47] Zuback JS, Moradifar P, Khayat Z, Alem N, Palmer TA. Impact of chemical composition on precipitate morphology in an additively manufactured nickel base superalloy. J Alloys Compd 2019;798:446–57. https://doi.org/10.1016/j.jallcom.2019.05.230.
[48] Kreitcberg A, Brailovski V. Effect of Fe and C contents on the microstructure and high-temperature mechanical properties of IN625 alloy processed by laser powder bed fusion. Materials 2022;15:6606. https://doi.org/10.3390/ma15196606.
[49] Liu A, Yang C, Wang F, Cheng C, Yang L, Du M, Lai B, Deng Q, Shao X, Liu Y, Luo R. Optimization of mechanical properties and corrosion resistance in cold-rolled Inconel 625 alloy by recrystallization annealing. Mater Lett 2026;407:140081. https://doi.org/10.1016/j.matlet.2026.140081.
[50] Deng D, Peng RL, Brodin H, Moverare J. Microstructure and mechanical properties of Inconel 718 produced by selective laser melting: sample orientation dependence and effects of post heat treatments. Mater Sci Eng, A 2018;713:294–306. https://doi.org/10.1016/j.msea.2017.12.043.
[51] Li B, Han K, Lek YZ, Zhou K. Effects of heat treatment on the microstructure and mechanical properties of Inconel 725 prepared by laser-directed energy deposition and laser-powder bed fusion. Mater Sci Eng, A 2026;950:149499. https://doi.org/10.1016/j.msea.2025.149499.
[52] Zhou L, Peng Z, Hu Z, Liu J, Chen J, Ren Y, Niu Y, Qiu W, Chen W, Li C. Grain morphology and mechanical properties tailoring of Inconel 625 alloy fabricated by laser powder bed fusion. Adv Eng Mater 2024;26. https://doi.org/10.1002/adem.202301785.
[53] Marchese G, Piscopo G, Lerda S, Salmi A, Atzeni E, Biamino S. Heat-treated Inconel 625 by laser powder bed fusion: microstructure, tensile properties, and residual stress evolution. J Mater Eng Perform 2024;33:6825–34. https://doi.org/10.1007/s11665-024-09235-7.
[54] Dubiel B, Gola K, Staroń S, Pasiowiec H, Indyka P, Gajewska M, Zubko M, Kalemba-Rec I, Moskalewicz T, Kąc S. Effect of high temperature annealing on the microstructure evolution and hardness behavior of the Inconel 625 superalloy additively manufactured by laser powder bed fusion. Arch Civ Mech Eng 2023;23:249. https://doi.org/10.1007/s43452-023-00787-4.
[55] Hu Y, Lin X, Li Y, Ou Y, Gao X, Zhang Q, Li W, Huang W. Microstructural evolution and anisotropic mechanical properties of Inconel 625 superalloy fabricated by directed energy deposition. J Alloys Compd 2021;870:159426. https://doi.org/10.1016/j.jallcom.2021.159426.
[56] Marchese G, Aversa A, Bassini E. Microstructure and hardness evolution of solution annealed inconel 625/TiC composite processed by laser powder bed fusion. Metals 2021;11:929. https://doi.org/10.3390/met11060929.
[57] Keya T, Bikmukhametov I, Shmatok A, Harvill G, Brewer LN, Thompson GB, Andurkar M, Thompson SM, O'Donnell V, Gahl J, Prorok BC. Evolution of microstructure and its influence on the mechanical behavior of LPBF Inconel 625 upon direct aging. Manuf Lett 2023;35:732–42. https://doi.org/10.1016/j.mfglet.2023.09.009.
[58] ASTM Standard G102-89(2015)e1 standard practice for calculation of corrosion rates and related information from electrochemical measurements, (n.d.). https://doi.org/10.1520/G0102-89R15E01.
[59] Carrozza A, Lorenzi S, Carugo F, Fest-Santini S, Santini M, Marchese G, Barbieri G, Cognini F, Cabrini M, Pastore T. A comparative analysis between material extrusion and other additive manufacturing techniques: defects, microstructure and corrosion behavior in nickel alloy 625. Mater Des 2023;225:111545. https://doi.org/10.1016/j.matdes.2022.111545.
[60] Mishra R, Imam M. Optimization of post-deposition heat treatment conditions to improve tribological, corrosion, and mechanical properties in direct energy deposited IN625® alloy. Mater Charact 2025;228:115412. https://doi.org/10.1016/j.matchar.2025.115412.
[61] Frankel GS. Pitting corrosion of metals: a review of the critical factors. J Electrochem Soc 1998;145:2186–98. https://doi.org/10.1149/1.1838615.
[62] Paranthaman D Poosapadi, Sailesh A, Sharma V, Singh R, L RB, Arun KK, Ravichandran M, Senthil TS. Role of heat treatment in enhancing microstructure and properties of Inconel 625 manufactured by directed energy deposition using wire arc. J Alloys Metall Syst 2025;9:100147. https://doi.org/10.1016/j.jalmes.2024.100147.
[63] Skobir Balantič, D. A., Donik, Č., Žužek, B., Podgornik, B., Kocijan, A., & Godec, M. (2026). Dataset for a publication "influence of build orientation and heat treatment on mechanical, tribological, and corrosion performance of LPBF Inconel 625" [data set]. Zenodo. https://doi.org/10.5281/zenodo.18605408, (n.d.).